Martin Steger, BSc

A Method for Flexible Camera Calibration and Lens Aberration Correction for Fixed Focal Length Lenses using Monochromatic Illumination

Master's Thesis

to achieve the university degree of

Diplom-Ingenieur

Master's degree programme: Telematik

submitted to

Graz University of Technology

Supervisor

Ao.Univ.-Prof. Dipl.-Ing. Dr.techn. Axel Pinz

Institute of Electrical Measurement and Measurement Signal Processing
Head: Univ.-Prof. Dipl.-Ing. Dr.techn. Georg Brasseur

Graz, August 2018

Affidavit

I declare that I have authored this thesis independently, that I have not used other than the declared sources/resources, and that I have explicitly indicated all material which has been quoted either literally or by content from the sources used. The text document uploaded to TUGRAZonline is identical to the present master's thesis.

Date	Signature

Acknowledgement

Danksagung:

Es gibt viele Menschen die dazu beigetragen haben, dass ich hiermit - doch noch mit etwas Stolz - diese Arbeit als Abschluss meines Studiums präsentieren kann. Manchmal laufen die Dinge im Leben anders, als man sich das am Anfang vorstellt und mein Weg war mit Sicherheit kein Klassischer. Damit habe ich gelernt, dass gerade dann, wenn man es braucht oft eine helfende Hand kommt und man auch selber mehr vom Leben hat, wenn man nicht nur stur auf die eigenen Ziele schaut. Aber an dieser Stelle ist es an mir, mich bei all jenen zu bedanken, die mir, auf die eine oder andere Weise, durch die Zeit des Studiums geholfen haben.

Als erstes möchte ich Herrn Professor Axel Pinz danken. Er hat diese Arbeit betreut und war auch bereit die Aufgabe als Mentor zu übernehmen. Ich bin der Meinung, dass der Einsatz deutlich über das ging, was ich als seine Pflicht gesehen hätte und seine Beiträge und seine Geduld (auch bezüglich der englischen Umsetzung der Arbeit) waren eine sehr große Hilfe. Dafür bin ich außerordentlich dankbar. Danke auch dem Personal des Instituts für Elektrische Messtechnik und Messsignalverarbeitung, das ich mit diversen Fragen löchern konnte oder um Hilfe bezüglich Organisation und Konstruktion bitten konnte. Dann möchte ich mich noch bei all den Lehrenden bedanken, die das Vermitteln von Wissen nicht nur als lästige Nebenaufgabe sehen und damit das Studium interessant machen.

Außerdem möchte ich meinen Eltern und meinen zwei Brüdern danken, dass sie mich auf meinem manchmal doch recht kurvigen Weg unterstützt haben und mir das Leben damit doch des Öfteren erheblich erleichtert haben. Ein großes Danke gebührt auch meiner Freundin. Durch meine Vorgehensweise war von ihrer Seite doch ein deutlich höherer Einsatz vonnöten, als das sonst der Fall gewesen wäre und sie hat mir den Weg

auf vielerlei Art verschönert. Natürlich möchte ich mich auch bei meinen Freunden bedanken. Bei denen die ich im Studium kennengelernt habe und die mich dort über kürzere oder längere Wege begleitet haben, aber auch bei jenen Freunden, die ich über die Jahre in Graz sehr wenig gesehen habe und dann trotzdem immer willkommen war.

Vielen, vielen Dank!

Damit bleibt mir nur mehr den Lesern und Leserinnen viel Spaß zu wünschen und ich hoffe es findet sich für jeden und jede das eine oder andere interessante Detail in dieser Arbeit.

Abstract

Current methods of camera calibration and aberration correction can only be applied to a specific set of lens settings. This substantially reduces the flexibility with which these methods can be used in practice. The aim of this thesis is to minimize such constraints and to develop an approach that can be used for online calculation in a camera.

A fixed focal length is used in order to eliminate the factor of internal lens rotation and thus reduce the complexity to a level suitable for the scope of this thesis. Monochromatic illumination is used, which allows for very clear evaluation of chromatic effects. Focus and aperture are very important settings for the quality of an acquired image. Therefore, the applied methods are evaluated with respect to these settings. Distortion, chromatic aberration and vignetting are discussed because of their importance in image acquisition and the fact that they can be modeled by radial models, which allows for effective treatment using well known methods.

These methods are modified and expanded to identify and address the parameters that need to be interpolated and used to develop an effective way to acquire the necessary sample points. An approach using four linear and two nonlinear parameters is applied for lens distortion and chromatic aberration correction and a model using three coefficients for vignetting correction. It is shown that the interpolation of these parameters leads to a significant improvement in image quality. The results illustrate the importance of adjusting the parameter set appropriately if the focus or aperture of the lens are changed.

Kurzfassung

Aktuell kann eine Kamera Kalibrierung oder eine Korrektur von Linsenfehler nur für eine Kombination von Kamera und Objektiv für eine bestimmte Einstellung bestimmt werden. Dies hat einen erheblichen Einfluss auf die allgemeine Anwendbarkeit dieser Methoden. Das Ziel dieser Arbeit ist es diese Einschränkungen zu reduzieren und eine Methode zu entwickeln, die es erlaubt bei einer Änderung einer Einstellung, dies sofort in der Kamera zu berücksichtigen.

Die Verwendung der fixen Brennweite erlaubt es den Einfluss, der sich im Objektiv bewegenden und rotierenden Linsen, zu eliminieren, was eine Beurteilung der Daten erheblich erschweren würde. Außerdem wird eine monochromatische Beleuchtung verwendet. Dies erlaubt eine genaue Evaluierung der chromatischen Effekte.

Bei einem Objektiv sind die Fokus- und Blendeneinstellung wesentliche Einstellungsmöglichkeiten, welche die Qualität des Ergebnisbildes beeinflussen. Deswegen ist es entscheidend, dass die angewendeten Methoden in Bezug auf diese beiden Einstellungen untersucht werden. Neben der Kamerakalibrierung werden Methoden für die Linsenverzeichnung, die chromatischen Aberration und die Vignettierung diskutiert. Alle diese Methoden können mit einem radialen Modell modelliert werden, was eine sehr effektive Bearbeitung mit bewährten Verfahren erlaubt.

Das Ziel ist es diese Verfahren so zu modifizieren und zu erweitern, dass eine effiziente Methode entsteht, die es ermöglicht die notwendigen Paramater zu identifizieren und für diese Parameter die passende Art der Interpolation zu finden. Das Ergebnis ist eine Vorgehensweise, die vier lineare und zwei nichtlineare Parameter verwendet und interpoliert, um die Linsenverzeichnung und die chromatische Aberration zu korrigieren. Für die Korrektur der Vignettierung wird ein Modell mit drei Koeffizienten verwendet. Die

Experimente zeigen eine signifikante Reduktion des Rückprojektionsfehlers unter Verwendung der interpolierten Parameter. Dies zeigt wie wichtig es ist bei einer Änderung der Fokus- oder Blendeneinstellung eines Objektives diese Änderung zu berücksichtigen.

Contents

List of Figures

List of Tables

1. Introduction

Digital cameras are used in nearly all areas of life nowadays. Image quality therefore, is naturally important. A major factor of image quality is the lens of the camera. While a lot of problems can be mitigated with sophisticated lens design this can lead to very expensive lenses and most of the time there are some residuals. An alternative way to solve this problem is to post process the image. This can be done for all lens aberrations to a different degree. These aberrations can be divided into different classes: monochromatic aberrations, chromatic aberration and effects which have their origin in the design and placement of the lens, namely vignetting and highlights like flares.

Camera calibration is required for image-based measurement and can be used to project a point in the world into the image. A single calibrated camera already can be used to measure angles between lines of sight. By using a second camera or additional information calibrated cameras can be used to acquire 3D data. Additionally, the calibration information is necessary as basis for some of the mentioned aberration correction algorithms.

The research done to solve the problems of aberration correction or camera calibration is considerable but to my knowledge there is no method which tries to combine this knowledge to a point where all these methods support each other for an overarching method. Another problem is that a parameter set of such a camera calibration or aberration correction is only valid for a very specific camera setting. The change of the focus or the aperture setting of a lens influences the resulting image significantly but to which degree a change of these settings influences the result of a camera calibration or aberration correction is unknown.

This leaves a considerable gap in the usability of these methods because in many applications these settings need to be adjusted to fit the current

situation. My goal in this thesis is to fill a notable portion of this gap. I focus my research on well known methods which solve a single problem and create and refine experiments to examine how significant the influence of a lens setting is. The next task is to examine if it is possible to find a method which takes this influence into account and, therefore, allow a flexible use of a method so that it can be used in a camera to calculate an appropriate camera calibration and image correction respecting each setting.

While it would be nice if solutions for every part of the problem could be presented, the large scope of this task forces me to some constraints. Therefore, only algorithms are considered which offer the possibility to be applied immediately after the image is taken with only reasonably short waiting time for a user. The second restriction is to only use lenses with a fixed focal length. In a lens with variable focal length (zoom lens), the internal lenses usually are rotated and because these lenses can not be perfectly aligned or crafted this can cause side effects which are very hard to isolate and, therefore, would complicate the evaluation significantly. The last premise is to only use monochromatic illumination. But all the experiments are done for red, green and blue. Therefore, this can be used to an advantage for a very clear evaluation how the color (wavelength λ) of light influences the results.

Problem Statement: Which settings of a lens have a significant influence on camera calibration and aberration correction? Is it possible to determine and use the resulting parameters effectively to have a valid camera calibration and aberration correction in (soft) real-time for a flexible use of these settings.

In this thesis, I follow the traditional approach to calculate the models by the means of point correspondences. To obtain these point correspondences a coordinate measurement machine (CMM) is used. Generally a CMM is used to sense the position on the surface of an object with extreme accuracy (micrometers), using a probe. This accuracy is utilized for the experiments, but instead of the probe a marker is fixed on the grapple and the positioning is done for a predefined model. The markers can be split into two types: passive and active markers. A passive marker gets illuminated externally, while an active marker is a light source on its own. The illumination is done using different LEDs and is controlled by an X-20 cpu unit manufactured

by B&R Automation. This X-20 is an industrial control unit which allows to switch on the LEDs exactly as required. The images are acquired by a Basler camera, which takes a monochromatic image with a resolution of 1920×1200 pixels. For this camera three different lenses manufactured by Azure Photoncis are used in the experiments. Two of these lenses are made with a fixed aperture, both with an f-number (also called f-stop) of four. These two lenses have a focal length of 8 mm and 16 mm. To evaluate the influence of the aperture, the third lens (16 mm) used allows to vary the f-number from 1.8 to 16. This equipment allows me to perform the needed experiments to determine how comprehensive point correspondences can be acquired effectively. This knowledge is used to obtain the required sample points, which enable me to develop an efficient method and to identify the necessary parameters and find appropriate interpolation models.

2. Background

To ease the navigation in this vast topic, the background is split into subtopics. First a brief overview over camera calibration is given, followed by lens aberrations, which are divided into the monochromatic aberrations and chromatic aberrations. At last the vignetting effect is discussed.

2.1. Camera Calibration

"Camera calibration in the context of three-dimensional machine vision is the process of determining the internal camera geometric and optical characteristics (intrinsic parameters) and/or the 3-D position and orientation of the camera frame relative to a certain world coordinate system (extrinsic parameters)..." [43]. For many applications in the field of computer vision it is a prerequisite to calibrate the camera before further methods can be applied. Therefore, a large number of different approaches to calibrate a camera were developed over the years. As described by Zhang [48], these methods can be classified into two categories: photogrammetric calibration and self-calibration. While photogrammetric (see appendix A.1 for definition) calibration needs very precise knowledge of the 3D geometry self-calibration uses the information of multiple images in a static scene to calculate the parameters. Self calibration has improved over the years but there are many parameters to estimate, which can be problematic, but it can be an attractive alternative for suitable problems.

The model such a camera calibration builds on is the pinhole camera, which is shown in figure 2.1. C describes the center of projection or camera center, which is the origin of the camera coordinate system. The point where the perpendicular line through the center of projection crosses the image plane

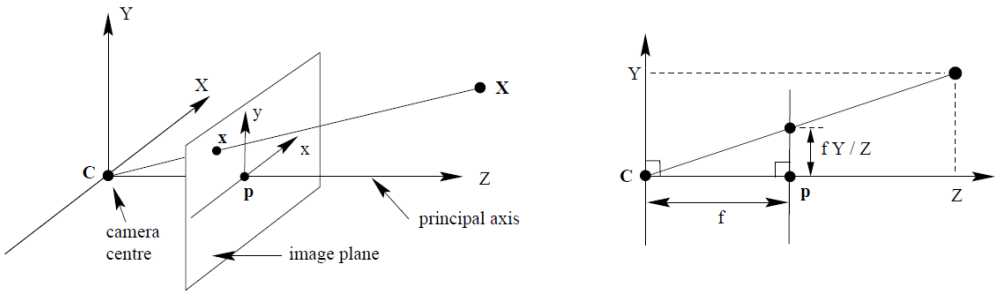

Figure 2.1.: Image, of the pinhole camera model, taken from [22]. **C** denotes the center of projection (camera center), **p** the principal point and **f** the focal length. Image coordinates are denoted as x and y and the world coordinates X, Y and Z

is known as principal point $\boldsymbol{p}$. This point also is denoted as $\boldsymbol{c}$, a notation I use for the rest of my thesis. The focal length $\boldsymbol{f}$ marks the distance of the image plane to the center of projection. This method builds on algebraic projective geometry and, therefore, many algebraic methods can be applied.

The foundation of the method is the 3×4 projection matrix $\boldsymbol{P}$, which can be used to project a 3D point (world coordinate) $\boldsymbol{X}$ into an image, which results in the 2D point $\boldsymbol{x}$ (equation 2.1). Although the matrix is of the dimension 3×4 it only has eleven degrees of freedom. The twelfth parameter is the scale parameter, which is not linearly independent. A point always describes a ray and, therefore, additional information is needed to determine the location on this ray. The projection matrix itself can be decomposed into the internal and external parameters. There are three directions in which a camera can be moved or tilted, therefore, there are six external parameters. Three different angles and three translation parameters, which cover six degrees of freedom of **P**. These six external parameters can be described in the 3×3 rotation matrix $\boldsymbol{R}$ and a translation vector $\boldsymbol{t}$. Instead of the translation also a position in respect to the world coordinate system $-\tilde{\boldsymbol{C}}$ can be used. The internal parameters or interior parameters are entries of the camera (or calibration) matrix $\boldsymbol{K}$ (equation 2.3). This matrix is an upper triangle matrix and its entries describe the remaining five degrees of freedom of $\boldsymbol{P}$. The five components are horizontal focal length f_x, the vertical focal length f_y and the skew s, which describes the angular deviation of perpendicular image axes. The last two components are the two coordinates

of the principal point c_x and c_y. The decomposition of $\boldsymbol{P}$ into the above mentioned components is given by equation 2.2.

$$\mathbf{x} = \mathbf{P} \cdot \mathbf{X} \tag{2.1}$$

$$\mathbf{P} = \mathbf{KR} \cdot [\mathbf{I}| - \tilde{\mathbf{C}}] \tag{2.2}$$

$$\mathbf{K} = \begin{bmatrix} f_x & s & c_x \\ 0 & f_y & c_y \\ 0 & 0 & 1 \end{bmatrix} \tag{2.3}$$

To ease the calculation it is beneficial to use homogeneous coordinates. These homogeneous coordinates add a dimension to each vector containing a scale factor and change the vector from Euclidean space into projective space. This leads to an equivalence class of vectors. For a clearer distinction inhomogeneous coordinates are often marked with a tilde on the top. In equation 2.4 and 2.5 it can be seen how this affects a 2D and a 3D vector. If the scale factor w (or W) equals one, the other values remain unchanged, in reference to the Euclidean format.

How important it is to normalize the data and not just blindly apply any algorithm on the given point data is shown in [17]. The result differs strongly although the same data is used. Without a normalization the result can be nearly useless due to numerical problems. In equation 2.6 it can be seen how the proposed normalization factor fac_{norm} can be calculated. The approach builds on the fact that a mean pixel index of $[1, 1]$, which equals a mean vector length of $\sqrt{2}$, leads to a numerically favorable setup.

$$\tilde{\mathbf{x}} = \begin{bmatrix} \tilde{x} \\ \tilde{y} \end{bmatrix} \quad \Rightarrow \quad \mathbf{x} = \begin{bmatrix} x \\ y \\ w \end{bmatrix} \tag{2.4}$$

$$\tilde{\mathbf{X}} = \begin{bmatrix} \tilde{X} \\ \tilde{Y} \\ \tilde{Z} \end{bmatrix} \quad \Rightarrow \quad \mathbf{X} = \begin{bmatrix} X \\ Y \\ Z \\ W \end{bmatrix} \tag{2.5}$$

$$fac_{norm} = \sqrt{2} \cdot \frac{1}{N} \sum_{i=1}^{N} \sqrt{x_i^2 + y_i^2} \tag{2.6}$$

To calculate the 3×4 projection matrix $\boldsymbol{P}$ the direct linear transform (DLT) [1] is applied, which requires an equation system of the form $\boldsymbol{A}\boldsymbol{p} = \mathbf{0}$. This can be achieved by calculating the cross product of a point with itself whose result is the zero vector, equation 2.7. Substituting one point $\boldsymbol{x}$ leads to equation 2.8, which can further be used to build the needed matrix $\boldsymbol{A}$ as seen in equation 2.9. Note that $\boldsymbol{P}_i$ is i-th row of the matrix $\boldsymbol{P}$. Each point n gives three equations but only two of them are linearly independent and as a consequence one equation has to be omitted, usually the third [42], which cuts the last row out of matrix $\boldsymbol{A}$. To calculate all eleven free parameters of $\boldsymbol{P}$ (the twelfth is the arbitrary scale factor) at least five and a half point correspondences are needed, which in reality naturally means to use six. The resulting matrix is of the size $2n \times 12$. By using six points to solve the equation system for $\boldsymbol{P}$ this will result in a 12×12 matrix. To improve the stability of the result, it is favorable to use more then six points and, therefore, use a considerably overdetermined equation system. The singular value decomposition (SVD, see appendix A.1) can be used to calculate the result.

$$\mathbf{x} \times \mathbf{x} = \mathbf{0} \tag{2.7}$$

$$\mathbf{x} \times \mathbf{P}\mathbf{X} = \mathbf{0} \tag{2.8}$$

$$\begin{bmatrix} \mathbf{0}^T & -w_i\mathbf{X}_i^T & y_i\mathbf{X}_i^T \\ w_i\mathbf{X}_i^T & \mathbf{0}^T & -x_i\mathbf{X}_i^T \\ -y_i\mathbf{X}_i^T & x_i\mathbf{X}_i^T & \mathbf{0}^T \end{bmatrix} \cdot \begin{bmatrix} \mathbf{P}_1^T \\ \mathbf{P}_2^T \\ \mathbf{P}_3^T \end{bmatrix} = \mathbf{0} \tag{2.9}$$

The desired matrix $\boldsymbol{K}$ can now be calculated by applying an RQ-decomposition (see appendix A.2) of the matrix $\boldsymbol{M}$ (as part of $\boldsymbol{P}$ as seen in equation 2.13) into a rotation matrix $\boldsymbol{R}$ and the camera matrix $\boldsymbol{K}$. By using the SVD to calculate $\boldsymbol{P}$, the result is optimal with respect to an algebraic error but does not minimize a geometrical meaningful error. To improve the geometric result an iterative algorithm which minimizes the reprojection error $\mathbf{e}$ (equations 2.11,2.12) can be used. Usually instead to optimize the whole rotation matrix $\boldsymbol{R}$ only the three corresponding Euler Angles are calculated and optimized. For $\boldsymbol{K}$, where all parameters are linear, most of the time at least four of the the five parameters are used in the optimization. The skew is often omitted because in modern cameras the impact is normally very small. After the desired parameters are chosen, an iterative optimization algorithm like the Levenberg-Marquardt algorithm can be used to optimize these parameters and after that the resulting $\hat{\boldsymbol{R}}$, $\hat{\boldsymbol{K}}$ $-\hat{\tilde{\boldsymbol{C}}}$ are used to calculate the $\hat{\boldsymbol{P}}$ until the $\hat{\boldsymbol{P}}$ which minimizes the reprojection error and, therefore, represents $\boldsymbol{P}$, is found. If the model needs nonlinear parameters, like when the lens distortion is considered, these parameters have to be included and the calculation of the reprojection error adapted. The last step is to calculate the denormalized $\boldsymbol{P}$ to fit the original coordinates.

As a closing remark I like to emphasize that because the measurement unit in the image is pixel the results are in pixel as well. To obtain physical values the results need to multiplied with the pixel size of the image sensor.

$$\hat{\mathbf{x}}_i = \hat{\mathbf{P}} \cdot \mathbf{X}_i \tag{2.10}$$

$$e_i = ||\mathbf{x}_i - \hat{\mathbf{x}}_i||_2 \tag{2.11}$$

$$\mathbf{P} = \min_{\hat{\mathbf{P}}} \sum_i e_i^2 \tag{2.12}$$

$$\mathbf{P} = [\mathbf{M}| - \mathbf{M}\tilde{\mathbf{C}}] \tag{2.13}$$

2.2. Lens Aberrations

There are different categories of aberrations in an optical system which have to be addressed. The first category are inherent aberrations of the glasses used: Deviations the light rays take from the ideal path. The results are geometrical errors and blur effects. The category can be split in monochromatic and chromatic aberrations. The second category are aberrations caused by the design of a lens: vignetting and flare effects. While vignetting will always occur, especially at low f-numbers, flare effects can easily be avoided in a controlled measurement setup. Therefore, flares are not considered in this thesis and the problem is more likely to fit an approach like machine learning, where the lost information due to the flare can be reconstructed.

2.2.1. Monochromatic Aberrations

The dual nature of light, wave and particle, leads to different models which fit different aspects. The wave model of Huygens states that every wave generates an infinite number of new waves along its path. This can be very useful to model certain effects like reflection, diffraction and refraction but to calculate the major properties of a lens usually simpler models are sufficient. A lot of good approximations can be done using geometrical optics, which uses a first order model to calculate the light rays. This is the common model which is taught in education. An expansion is the third order model by Seidel [38] whose results ares five aberrations; spherical aberration, coma, astigmatism, curvature of field and the lens distortion. As a side note it is worth to mention that technically speaking defocus can be considered a monochromatic aberration as well.

The **spherical aberration** is the effect that a change of refraction towards the rim of the lens causes a change of the focal point and, therefore, the rays intersect the optical axis at different places. Outer rays intersect in front (positive spherical aberration) or behind (negative spherical aberration) the specified focal point. **Astigmatism** is the effect that the lens is not homogeneous and, therefore, for rays outside the optical axis the horizontal and vertical focal point differs causing blur. The **coma** aberration got its name from the fact that this aberration effect looks like a coma or comet.

If parallel light rays hit the lens at an oblique angle, a variation in magnification causes a blur with the described shape. The **curvature of field** or sometimes Petzval field curvature describes the effect that the image can not be focused on a flat plane but is rather mapped along a curve. Therefore, only small parts of the image are perfectly in focus. The last and probably most important of these Seidel aberrations for image correction is the **lens distortion**. The lens distortion is generated due to a spatial change of the magnification. The result is that the image is not linearly proportional to the distance of the optical axis. It is usually classified into two categories. Pincushion lens distortion, which occurs if the magnification increases with the distance from the optical axis and barrel lens distortion which occurs if the magnification decreases. The lens distortion is usually modeled using radial and tangential components in dependence of even exponents of the radius r. This was first published by Brown [6] and most of the solutions to correct this aberration use at least the radial part of the model. Equations 2.15 and 2.16 describe how the undistorted coordinates x_u and y_u are moved from their distorted position x_d and y_d. This is done by using three radial parameters r_1, r_2, r_3 and three tangential parameters t_1, t_2, t_3. The radial parameters correct the radial deviation in respect of the distance of the radius from the image center. The tangential parameters correct the decentering aspect. These non-linear parameters are usually calculated using an iterative optimization algorithm like Levenberg-Marquardt. While the diameter of the aperture has no direct effect on the lens distortion, the position has. An aperture in front of the lens leads to barrel lens distortion, an aperture in the back of the lens to pincushion lens distortion ([23], chapter 6).

$$r = \sqrt{(x_u - c_x)^2 + (x_u - c_y)^2} \tag{2.14}$$

$$x_d = x_u(1 + r_1 r^2 + r_2 r^4 + r_3 r^6) + (2t_1 x_u y_u + t_2(r^2 + 2x_u^2)(1 + t_3 r^2) \tag{2.15}$$

$$y_d = y_u(1 + r_1 r^2 + r_2 r^4 + r_3 r^6) + (t_1(r^2 + 2y_u^2) + 2t_2 x_u y_u)(1 + t_3 r^2) \tag{2.16}$$

	Effect aperture	Effect image height
Spherical longitudinal	D^2	–
Spherical transversal	D^3	–
Coma	D^2	H
Astigmatism transversal	–	H^2
Astigmatism longitudinal	D	H^2
Field curvature transversal	–	H^2
Field curvature longitudinal	D	H^2
Distortion linear	–	H^3
Distortion percent	–	H^2

Table 2.1.: Monochromatic aberrations and their dependence ([39], chapter 3). The second column shows the influence of the aperture diameter D, the third column the influence of the so called "image height" or field size H (i.e. distance form the image center)

Spherical aberration, coma and field curvature are resolution errors and can be considered a convolution effect. Therefore, it is possible to use an appropriate point spread function and deconvolution to correct these aberrations. Unfortunately, a very large number of unknown parameters have to be considered and the result is strongly depended on the scene and for that reason it is critical to adjust the point spread function spatially. On the top due to the way a (de)convolution works even small errors in the model can result in very obvious artifacts aggravating this problem even further. As a side note I like to mention that the maximum obtainable resolution for a specific focal length f is always limited due to diffraction in dependence of the wavelength of light λ and the diameter D of the aperture (Airy disk: $D_{airy} = 2.44 \cdot \lambda \cdot k$ with f-number $k = \frac{f}{D}$).

How the five Seidel aberrations relate to image height (also field size) and the diameter of the aperture can be seen in table 2.1.

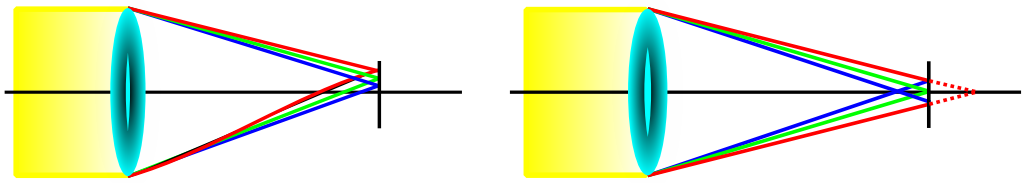

(a) Lateral CA (b) Longitudinal CA

Figure 2.2.: Effect of the lateral and longitudinal chromatic aberration. The lateral chromatic aberration is a difference in magnification and shows as displacement. The longitudinal chromatic aberration is the difference of the optimal focus for each color and shows as resolution error.

.

2.2.2. Chromatic Aberrations

The deviation of light from the optimal case in dependence of its color , which implies its wavelength, is known as chromatic aberration (CA). As seen in figure 2.2 the effect can be divided into two phenomena, which can be termed lateral and longitudinal or axial chromatic aberration ([23], chapter 6). The lateral chromatic aberration is an effect which occurs because of the difference of the magnification of different colors. In an image this can be perceived as color rims which get more evident the farther away from the image center. The longitudinal chromatic aberration blurs an image because each color has a different focal point. Therefore, the majority of colors will be slightly defocused and decrease the resolution. This effect does not change with the distance from the image center but is dependent on the aperture of the lens (table 2.2). To minimize the effect, achromatic doublets can be used, which usually optimize two wavelengths and usually consist of a concave flint glass element (high disperson) and a convex crown glass element (low dispersion). An alternative is a diffractive optical element.

2.2.3. Vignetting

There are different reasons for vignetting. In [16] these causes are categorized into four classes. First **natural vignetting** which refers to the radial falloff due to the geometry of optics. The effect is often modeled as function of the

	Effect aperture	Effect image height
Lateral chromatic aberration	–	H
Longitudinal chromatic aberration	D	–

Table 2.2.: Chromatic aberrations and their dependencies of the aperture diameter D and image height H([39], chapter 3).

cos^4 but this law can only be seen as an approximation. **Pixel vignetting** refers to the radial falloff due to angular sensitivity of a digital sensor. The photons with an oblique angle produce a weaker signal than at a normal angle. **Optical vignetting** refers to the radial falloff due to blocked light path inside the lens diaphragm. It is a function of the aperture and it is influenced by aperture size and shape. **Mechanical vignetting** is mentioned last, it refers to radial falloff due to light paths blocked by other elements of the camera; as an example filters and hoods.

It can be seen that all of these effects follow a radial falloff and the sum of all these effects produces what is generally known as vignetting. While each of these effects follows a specific model it is not necessary to correct each one separately. A radial model with even exponents as seen in equation 2.17 fits the problem as a whole very well. This vignetting function V in dependence of the radius r (equation 2.14) can be used with the appropriate α_i coefficients to correct an image. When the coefficients are calculated a simple multiplication of the pixel intensity I with the vignetting function $V(r)$ leads to the corrected value I_{cor} (equation 2.18). To calculate the α_i coefficients, pixel intensities of a reference image in dependence of the radial distance can be used. The prerequisite is that the reference image is taken of a target and illumination, which are completely homogeneous. Like with the lens distortion correction it is very important to normalize the data before use. The final result then strongly depends on the number of used coefficients and the quality of the reference image.

$$V(r) = 1 + \alpha_1 r^2 + \alpha_2 r^4 + \alpha_3 r^6 + \alpha_4 r^8 ... \tag{2.17}$$

$$I_{cor} = V(r) * I \tag{2.18}$$

3. Related Work

The structure in this chapter is similar to the background section 2 with a few differences. Camera calibration and the monochromatic aberrations are part of the first section mostly because a lot of work combines camera calibration and lens distortion correction. The second section covers work regarding chromatic aberration and the third and last section is about work relating to vignetting.

3.1. Camera Calibration and Monochromatic Aberrations

Seidel developed a third order model for optics in 1856 [38]. Based on this, the classification for the five monochromatic aberrations are made. Namely spherical aberration, coma, astigmatism, curvature of field and, for image acquisition usually most important, the lens distortion.

Based on previous work of A.E. Conrady [10], Brown published, what I would call the basic model for lens distortion in 1966 [6] and 1971 [5]. Lens distortion is modeled by a radial and and tangential model using the even exponents of the radius (see equations 2.15 and 2.16).

The need for camera calibration to map object space to image space was already noticed more then fifty years ago. Sobel [40] developed a camera calibration model for a camera and robot setup in 1974 and already distinguished between external and internal parameters. The main goal was to predict changes to save on expensive computations in image analysis.

Although starting off with very expensive cameras for very specific tasks like aerial mapping or metrology, nowadays cameras are getting cheaper

and cheaper and, therefore, there are more and more applications, which led to a constant research on the topic of camera calibration. In [9], an overview over the development of camera calibration up to 1998 is given. But as a consequence of the constant camera development which led to a steady increase in cameras, a lots of research was done and already in [33] a further evaluation is done, this time up to 2006. This paper focuses more on the comparison of the different approaches, which can be considered established today, and gives very useful overview of the topic. An other overview is given in [34] (2010) but there the focus is on the lens distortion models and which model is suitable for which type of lens.

Roger Tsai 1987 proposed a new technique [43] which was novel because it also could be used to calibrate off-the-shelf cameras and lenses. A target with a coplanar set of points was used to obtain the 3D world coordinates. The processing pipeline from 3D point to 2D image point starts with a rigid body transformation to estimate the rotation and translation, after that the perspective projection with pinhole geometry is used to calculate the focal length and at last the two radial lens distortion parameters and the scale factor are calculated. The principal point is simply assumed to be at the image center. The results are evaluated for three cases; monoview single plane, monoview multiplane and multiview.

In 1997 Heikkila and Silven proposed a four step method [25] which handles the calibration process as a whole. Until then the main research interest was in the fitting of the model. Step one is to apply the direct linear transform (DLT) from [1] to calculate the linear parameters. Step two briefly discusses the nonlinear parameter estimation and step four discusses the image correction. It is noted that there is no direct solution for the back-projection and if tangential and radial parameters are used no analytical solution exists. Step three discusses the importance of the correction of the perspective projection of circles, which are used as marker. This problem is valid for all 2D or 3D shapes.

Zhengyou Zhang developed a new flexible calibration technique [48] in 2000. The huge advantage is that it only requires a planar target without further reference, which makes expensive 3D targets unnecessary and, therefore, camera calibration a lot more accessible. Markers on this planar target have to be found in multiple poses but without the need to know the motion.

Using this data a homography can be calculated which can be used to calculate the camera calibration in a closed form, which is related to the absolute conic. The result is an algebraically optimal solution which has to be followed up by a non-linear optimization to add the lens distortion and give the result geometrical meaning. It is noted that in this approach parallel planes lead to a degenerate configuration and therefore do not provide additional constraints. Hartley extended the method 2007 with a non-iterative approach to also fit fish eye lenses [20].

The methods by Tsai, Heikkila and Zhang had and have a large impact how camera calibration is done but there is a great number of other interesting methods. A few of them I like to summarize.

An implicit method where the camera is calibrated without explicitly calculating the physical parameters using two planes is shown in [45]. The approach uses projection and back projection and gives good results but is calculation intensive. A combination with a linear method generates an explicit camera calibration.

Points are the first way to calculate the lens distortion. An other way is to exploit the fact that "Straight lines have to be straight", a fact that important that Devernay and Faugeras made it the title of their paper [11] in 2001. They developed a transformation which they used to correct video sequences based on different models. Some of these models also worked very well with wide-angle lenses. Edge detection is done to extract lines, which are used to calculate the parameters for the correction.

In 2013, an interesting self-calibration method for radial distortion is developed using epipolar lines. Epipolar lines which run through the center can be used to compute a camera calibration [4]. These lines stay straight through the radial distortion center and the calculations can be done without need for iterative optimization. With two views with the same lens distortion or three views from different lens distortions it is possible to calculate the result using a simple closed form. A drawback is that a circle with a very large radius is hard to distinguish from a straight line, therefore, this method works best for lenses with high lens distortion but it is stated this also needs an adjustment of the model.

Another approach for camera calibration is self-calibration. Hartley [18], in 1994 shows that it is possible to calculate a camera calibration by matching points using projective geometry and a rotating camera with no skew. At least two images are necessary but the accuracy increases using more images and in his experiments Hartley settles for three images to obtain reasonable results. The experiments show that a non-iterative approach already achieves good results. This can handle problems regarding local minima. Therefore, iterative optimization only should be used in need of extreme accuracy. An extended version [19] was published in 1997 stating that the required number of images to achieve an certain accuracy depends on the type of lens. Another self calibration method is shown in [32]. This paper also gives theoretical proof that the absence of skew is sufficient to allow a self calibration. It also discusses which boundary conditions to apply to optimize the trade-off between speed and generalization.

In 2011, Schmalz et al. [36] used the accuracy of digital displays to replace costly targets. The display is actively controlled and shows coded patterns which constitute a suitable calibration target. Two years later, in [26], a digital display was used to display sinusoidal fringe patterns which enable an approach called virtual defocusing to reduce the effect of the pixel grid of the display. The authors reported a reprojection error of 0.0067 pixels. Both methods need multiple poses of the display but emphasize on the advantage of flexibility which digital displays offer.

While very complex, there are solutions to correct the resolution aberrations. This can be done using a point spread function (PSF) and deconvolution, but these calculations are very expensive and the scene has to be very well known because otherwise artifacts are generated. For example this approach works very well in astronomy ([44], chapter five).

An other way to estimate the PSF is shown in [27]. Sharp edges are used to predict the necessary kernels for the deconvolution. The limitation of this method is that only kernels with one peak can be detected because the method is based on edges. But within the limits, it can also be used to correct chromatic aberration.

A completely different approach is shown in [37]. There, a custom lens only using a single lens element is used to estimate a spatially varying kernel for deconvolution.

3.2. Chromatic Aberration

Already in 1992, image warping between color channels was successfully applied to correct the chromatic aberration. In [3], this was compared to an active lens control approach where three images are taken with slightly different focus and zoom settings to compensate the optics. Significant advantages could be achieved, although the images used in 1992 only have a resolution of 338×388. In 2007, Mallon and Whelan [30] proposed a method where the image warping is expanded by a model which is fitted to the lateral chromatic aberration, thereby improving the result significantly.

Another promising approach to correct the chromatic aberration is to use wavelets. While related work, regarding wavelets for chromatic aberration correction generally seems to be preemptive, Fryskowska et al. [14] show that chromatic aberration can be detected and reduced. But they also state that no real images are used and only a few selected wavelets could be tested.

Monochromatic camera calibration data is used in [29]. A reference calibration for the green channel is done and used for the other channels. Only the horizontal and vertical focal length is adjusted in the calibration process.

Due to the difference in the effect of lateral chromatic aberration (misalignment) and longitudinal chromatic aberration (blur) many methods are designed to correct only one of these two aberrations. But there are methods which try to correct both forms of aberration.

The active lens control system from [46] states to correct both types of chromatic aberration, but the method needs an elaborate setup and therefore is not universally applicable.

In [28], the chromatic aberration was corrected only using a single image by a multiple step approach which uses a kernel that accounts for magnification and defocus. The kernel estimation builds on the detection of strong edges. Furthermore it is noted that camera sharpening increases the problem and, therefore, is included in the model. This results in nine chromatic aberration related parameters which have to be computed. Using the hardware available in 2007 processing the full model took about fifteen minutes for a high resolution image of 3072×2048 pixels.

Another method which claims to correct lateral and longitudinal chromatic aberration is shown in [8]. Differences in the color behavior at edges are analyzed and used. First edges without chromatic aberration are identified and afterwards edges which violate this condition are found. The correction is done by adjusting the color difference to be similar to the minimum of differences.

In [7], a method is proposed which considers the chromatic aberration a false color artifact which has to be removed. This has the advantage that no pre-calibration is needed. Lateral and longitudinal chromatic aberration introduce different but distinctive kinds of artifacts can be identified and filtered out after a transient improvement preprocessing.

In [41], the fact is used that usually one of the color channels is more focused and despite the difference in intensity the high level structures are mostly similar. This similarity is used to transfer pixel information through channels and blindly remove the chromatic aberration using the strong pixel wise correlation via deconvolution.

In 2012 different approaches were evaluated and compared in [31]. The methods are categorized into three types: methods which build on camera calibration of color separated images, methods which assume the magnitude of chromatic aberration as a function of the radial distance from the image center and proprietary software. The method with the best result was an approach using a cubic function of the radial distance from the image center, the second best was a method using camera calibration where every color has an independent image lens distortion model but a fixed camera.

3.3. Vignetting

There are different reasons for the vignetting effect. In [16], these are described in four categories: natural vignetting, pixel vignetting, optical vignetting and mechanical vignetting. All these categories are stated to follow a radial falloff. The correction of the vignetting effect does not yield new information per se but it is very obvious to the human eye and the effect can be interfering with post processing of an image. A simple example is a

threshold operation were the darker borders could get ignored because of the falloff.

In 1947 the validity of the cos^4 law of illumination is checked by Gardener who states that the effect in images is also influenced by the lens distortion and a function of the entrance and exit pupils of the aperture [15]. In [2] the cos^4 law and its effect on vignetting is also evaluated. In the evaluation a significant effect of differently shaped aperture pupils on the result is found. In addition, a light grid is used to achieve spatially varying PSF kernels.

The vignetting effect is also important in the area of image stitching. The difference in brightness when effected images are stitched together is very easy to spot.

In [16], a nonlinear objective function is used to calculate the coefficients for a radial model with even exponents. In [12], the same radial model is used but the coefficients are instead calculated by a linear method using propagation and back propagation to acquire the coefficients. For both methods the results are clearly enhanced images but there is no quantitative analysis shown. Therefore, it is not clear which method delivers better results.

Another model with the goal to be able to correct the vignetting effect using only a single image is shown in [49] [51] and [50]. All three papers by Zheng et al. are using a correction model which is split into two functions: an off-axis falloff illumination factor and a geometric factor. The difference is the acquisition of the parameters. All three publications use regularities which are present in an image. The first paper [49] is using segmenting, the second paper [51] uses the radial gradient symmetry which uses regularities in the statistical distribution and builds on the fact that vignetting always increases its skewness. The third paper [50] uses the radial gradient and semi circular tangential gradients to improve the result further.

In [47], a method using a scanline approach to save memory compared to the traditional lookup tables was proposed. A hyperbola is created for every line and the coefficients are saved to be used for correction.

4. Method

Looking at the different aberrations and the correction algorithms, it is obvious that not all are suited for an online approach. As an example the correction for resolution aberrations usually use an approach via deconvolution and are very scene dependent. Therefore, it is only possible to correct these effects for a very specific scene setting and the usage of massive processing power. This makes such methods unsuitable for a method which emphasis is to be fast and flexible.

Aberrations well suited for a fast online correction method seem to be the lens distortion, the lateral chromatic aberration and the vignetting. Firstly there are correction algorithms which are not too calculation intensive. Secondly they share the fact that for each of them, there are approaches, which are based on radial models. Hence, it is more likely to be able to utilize synergies. Therefore, the emphasis of this thesis is on these aberrations in addition to the camera calibration. The method as a whole focuses on the evaluation of effects based on the change of focus, aperture and wavelength of light. For the camera calibration, a photogrammetric approach is chosen because it can be done efficiently [13] and with the coordinate measurement machine excellent hardware is available. I follow the commonly used approach in camera calibration (e.g. [22],[40]) and calculate an initialization for the linear camera parameters (matrix $\mathbf{K}$), followed by an iterative optimization for all parameters. The chromatic aberration and lens distortion correction are built on the basics of the camera calibration. For the the vignetting effect, which needs a different approach, a digital display is used as light source.

4.1. Light Source and Illumination

To evaluate chromatic effects like the chromatic aberration or the influence of different wavelengths on the parameter set, using a monochromatic illumination, it is important to know the exact spectrum of the illumination. In the experiments, three different LED types are used; CREE XQE High Density LEDS in red, green and blue. Figure 4.1a shows the spectra from the data sheet. In figure 4.1b the data is obtained by a measurement using an Avantes Avaspec 2048 spectrometer. The measured data matches the data sheet very well and the spectrum of the different LEDs is narrow enough to be considered a monochromatic illumination. Because the LEDs differ in intensity at a fixed voltage there is the necessity to use different exposure times $t_{exp}$for each color setting. I used an approach were the exposure time was increased until a predefined area hit the maximum value of 255 and calculated a ratio, using red as reference color to calculate the exposure time for green and blue (equation 4.1). I used these LEDs for all monochromatic illumination and light source purposes.

$$t_{exp_{green}} = t_{exp_{red}} \cdot \frac{t_{max_{green}}}{t_{max_{red}}} \quad \text{and} \quad t_{exp_{blue}} = t_{exp_{red}} \frac{t_{max_{blue}}}{t_{max_{red}}} \tag{4.1}$$

For image acquisition, not only the difference of the different LED intensities is important. The distance of the marker from light source effects the brightness significantly. Therefore, after the lens settings are established the exposure time t_{ref} for the maximum working distance is determined. From this measurement the necessary factor for all other points is calculated as a function of the distance d_{mark} to the marker using the inverse square law (equation4.2).

$$factor_{distance} = \left(\frac{d_{mark}}{d_{ref}} \right)^2 \tag{4.2}$$

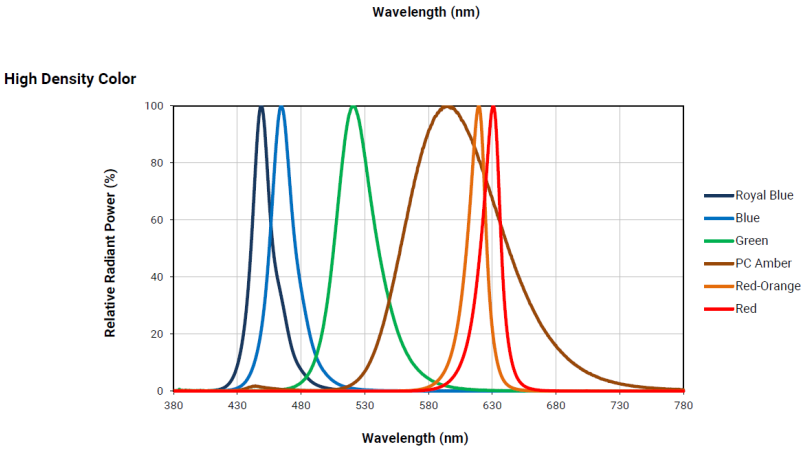

(a) Spectrum of the LEDs from the CREE datasheet.

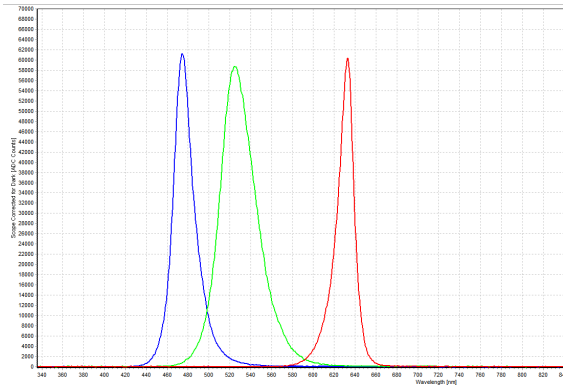

(b) Spectrum of the LEDs from measurement using the Avantes Avaspec 2048 spectrometer.

Figure 4.1.: Spectra of the used CREE LEDs.

4.2. Point Correspondences

To calculate the correction parameters, point correspondences are needed. A point correspondence represents a mapping of a 3D world coordinate to a 2D image coordinate. To obtain a meaningful camera calibration, it is important that the markers representing a coordinate in the world are placed accordingly. The positions of all markers can be considered a point cloud. To achieve good results all image areas have to be covered and depth information has to be available. However the details, how such a point cloud has to be generated, vary strongly depending on the requirements and, therefore, there are several different approaches. I used two different methods. The first one is used to establish meaningful results using well known methods from literature. The second method aims at a faster acquisition of the point correspondences. In all my experiments the point cloud is processed successively by placing a single marker using the coordinate measurement machine (CMM). The average time to process a point is about 20 seconds. The used measurement setup can be seen in figure 4.2. That said, it is also possible to use 2D or 3D targets containing multiple markers as long as the precise world coordinate of each marker is known and each marker can be assigned reliably to the corresponding position in the image.

In figure 4.3, the point cloud for the first method can be seen. The points are placed in a volume of a truncated pyramid according to the field of view of the camera. This volume is divided into several layers. Each layer consists of a number of points covering the corners and a grid in which the area inside is covered. The points in the grid are randomized accordingly in each grid volume in order to minimize the risk of numerical instability due to linear dependence. In the image, it can be seen that there are two different volumes for a close focus distance (10 cm) setting and a focus setting at the end of the specified working distance (70 cm). This difference can be significant and, therefore, the point cloud must be adjusted to ensure a good result for either setting. For that reason the used set contains corner points points along the rim, which are optimized for a close focus setting and a far focus setting. Using seven layers for a working distance of 10-70 cm this results in 224 points/images. A working distance of 10-50 cm with the same spacing will contain 160 points etc.. The point positions are the same for all processed focus distances. The reference exposure time at maximum work distance,

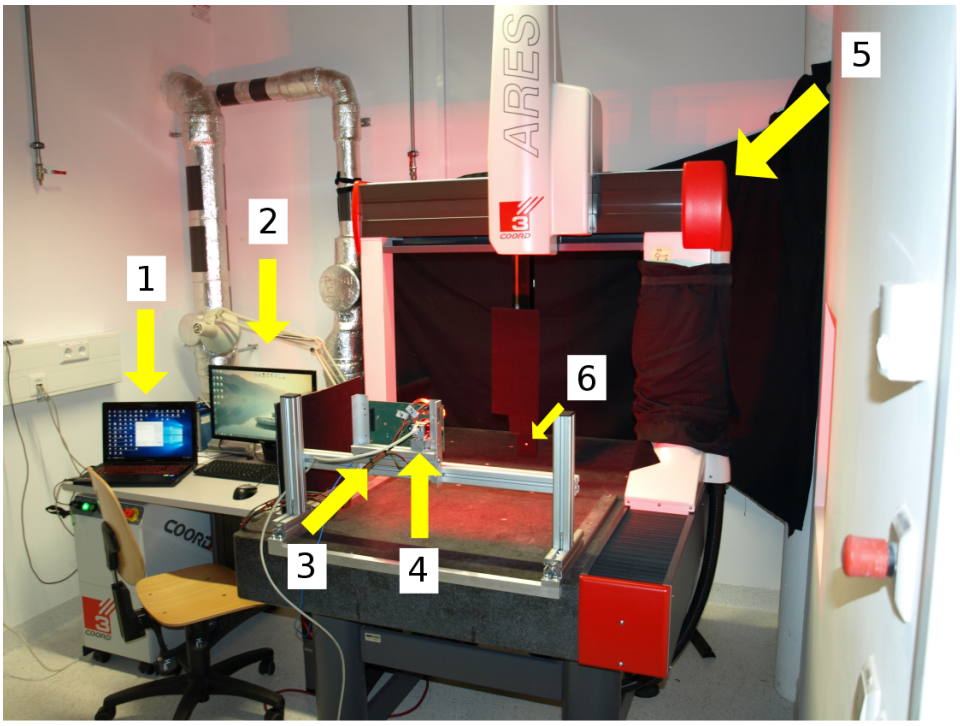

Figure 4.2.: Image of the measurement setup. The laptop (1) controls an X-20 unit to direct the setup and to save the images. The coordinate measurement machine (5) is controlled by a separate computer (2) to position the target (6) at very high accuracy. The RGB LED illumination for image acquisition with a passive target can be seen at (3). The camera (4) is mounted in the center of the LED board, which is used for the illumination.

which is used as reference distance d_{ref} differs and strongly depends on the focus setting. The close range focus setting of 10 cm needs 75000μs, the focus setting for 70 cm needs only 3500μs. The combined impact of distance, color and focus on the exposure time is very significant. This leads to an exposure time range from 300 to 75000 μs for the acquired images.

The point cloud for method two can be seen in figure 4.4. The amount of points is reduced and the layout would allow the usage of a 2D target with a known translation in one direction. For each layer four corner points, six points along the rim and twelve grid points are used. The points are not randomized and results have shown that the random placement is

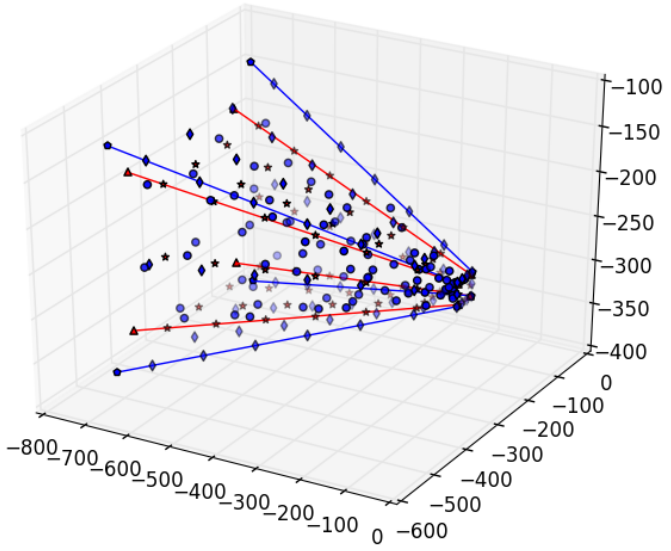

Figure 4.3.: An example of a truncated pyramid pointcloud. The red lines show the field of view for a focus distance of 10 cm, the blue lines for a focus distance of 70 cm. The stars and diamonds along the two borders mark the placed corner points. Inside the volume, points are placed along a grid and noise is added to randomize the positions. The axes represent X, Y and Z world coordinates in millimeter (CMM coordinate reference frame).

not necessary as long as there is a sufficient number of layers to provide additional depth information. Using only one layer, the problem is ill posed. The scale of an image can not be recovered, therefore, the focal length is unknown and no solution can be calculated. Using two layers, generally a solution can be calculated but sometimes numerical problems occur in the iterative optimization. But even if the numerical problems do not force a preemptive termination, the results for two layers are significantly worse compared to the first method with the truncated pyramid. For three and more layers, the numerical problems do not occur. The accuracy of the results depends on the number and the positions of the used layers. Details for typical results can be seen in table 4.1.

The shown configuration ensures the camera calibration and correction is valid for this volume of interest. If the layers are positioned accordingly, the accuracy of the results for three layers are in line with method one. For four or more layers the result does not improve anymore. In the ideal point setting, the results for three and more layers are the same up to the fifth decimal place but even with induced measurement errors the result does not improve significantly. Therefore, a three layer approach is chosen, which results in 66 points (images to take) for each processed focus distance. This is a big improvement compared to the 224 points of method one, but as a trade-off the point cloud has to be adjusted for each focus distance used. In figure 4.5, a suitable configuration of the planes for three layers is shown. As a rule of dumb an image should be usable a third in front of the focus point and two third behind the focus point. The details how the point clouds of the two methods compare can be seen in table 4.2. The reprojection errors for the two methods using two different test sets, which correspond to two different focus settings, can be seen in table 4.3. The results for method two, the three layer approach, are a little bit better. This can be explained by the fact that the correct centroid is harder to find, if the threshold is not set accurately, which is harder for a defocused marker and there are more images of defocused markers in method one. But overall, the accuracy is very similar for both methods and the results are very good.

	mean	min	max
1 layer	N/A	N/A	N/A
2 layers	81.354	0.001	1566.093
3 layers	0.294	0.001	1.344
4 layers	0.294	0.001	1.344

Table 4.1.: Comparison of typical results for the reprojection error for different numbers of layers using ideal (reprojection error free) points. One layer yields no results. The results for two layers are lacking but already good for three layers. Differences for third and fourth layer do not occur up to the fifth decimal place. The lens simulated is the Azure 8 mm S-Mount.

A number of quality criteria have to be fulfilled to ensure that markers can be reliably localized. A check for a plausible size, a ratio check, a compactness check and a check for a minimal needed intensity is done. The method is

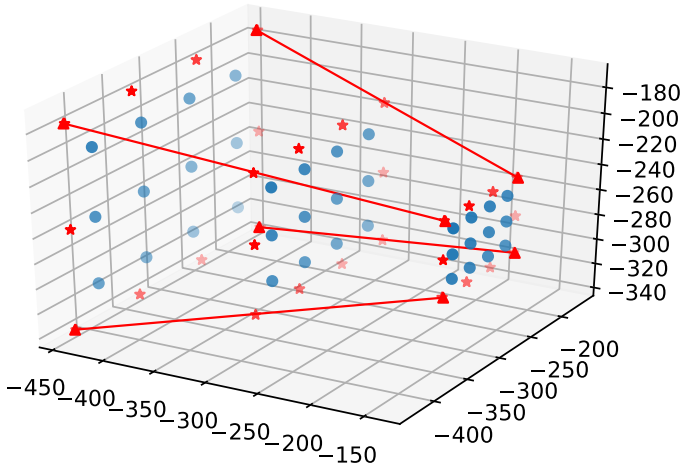

Figure 4.4.: An example of a three layer point cloud. The red lines show the field of view for the specified focus distance. The stars mark corners and points along the rim and the circles the grid points. The axes represent X, Y and Z world coordinates in millimeter.

repeated iteratively and the image is cropped each time until only a small border remains to eliminate all other external influences. The final review is to check the borders to verify the marker is complete. After this area of interest is identified, the center can be calculated by applying a threshold and calculating the centroid. The calculations used to extract the marker centroid $\mathbf{c}$ can be seen in equations 4.3,4.4 and 4.5 where m and n are the indices of the processed pixel, X and Y the size of the area of interest.

$\tilde{I}$ is the weight value, which is used for a pixel, which is above the threshold, N the sum of all these weight values. For circular markers a well working approach is to set all weights (pixel intensities) above the threshold to one. A more universal approach is to use normalized image intensities. Each intensity is divided by the maximum intensity, generating a value between zero and one for each weight. The normalization allows a more general handling of problems. The result of the centroid calculation is the position

	Method 1	Method 2
Corner points	2×4=8	4
Edge points	2×6=12	6
Grid points	12	12
Layers	7	3
Total points	224	66
Generated point clouds	1	1 per focus distance

Table 4.2.: Comparison of the accuracy of the point clouds to acquire the point correspondences. Method 1, the truncated pyramid and method 2 the three layer approach.

	Method 1			Method 2		
	mean	min	max	mean	min	max
Set 1: 30	0.66	0.07	2.2	0.33	0.06	0.73
Set 2: 30	0.49	0.05	1.63	0.32	0.05s	0.82
Set 1: All	0.54	0.02	1.71	0.31	0.01	0.96
Set 2: All	0.41	0.01	1.44	0.31	0.01	1.1

Table 4.3.: Comparison of the reprojection error of the point clouds to acquire the point correspondences. Method 1, the truncated pyramid and method 2 the three layer approach for seven measurements distances with two sets using two different focus settings. The results are compared using thirty and all point correspondences. Because the difference of the results for the different color channels is not significant the results are a combination of red, green and blue.

with sub pixel accuracy.

$$\tilde{I} = \frac{I}{I_{max}} \quad or \quad \tilde{I} = 1 \tag{4.3}$$

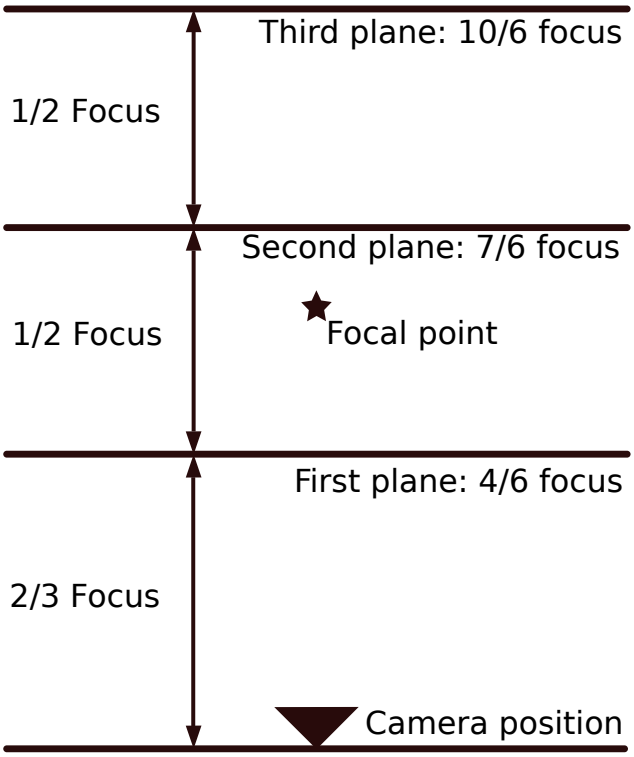

Figure 4.5.: A plane configuration for faster image acquisition. The concept allows the use of a 2D target with translation and, therefore, can also be done without a coordinate measurement machine.

$$c_x = \frac{1}{N} \sum_{m=1}^{X} \sum_{n=1}^{Y} \tilde{I} \cdot m \tag{4.4}$$

$$c_y = \frac{1}{N} \sum_{m=1}^{X} \sum_{n=1}^{Y} \tilde{I} \cdot n \tag{4.5}$$

4.2.1. Passive targets

Targets using markers which are illuminated by an external light source can be referred to as passive targets. Although all form of markers are possible,

the use of circular markers has been demonstrated to be very suitable for an exact localization [24]. An image of the marker I used can be seen in figure 4.6. The circle has a diameter of 4 mm which has proven to be best for a working distance from 5 to 70 cm. The need to find the center even strongly defocused at the end of the working distance leads to the usage of a very strong illumination. Therefore, all other areas are covered with absorptive material. The marker itself is made of white paperboard encircled by black velvet, which has shown to have better absorption properties than black paperboard or, even dull, printed black. The surface of the paperboard has to be on the same level as the velvet to prevent shadows. As the illumination is permanent the brightness in the image is controlled by the exposure time. In figure 4.7 two images of the setup with activated illumination can be seen.

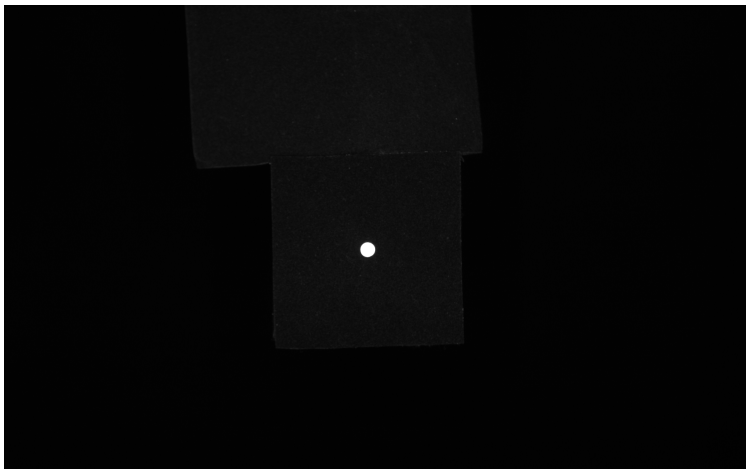

Figure 4.6.: Image of a passive circular target containing a single marker in central position. All surrounding and reflecting parts are covered in black velvet to simplify the center extraction.

Figure 4.8 shows six examples of images used to localize the position of the marker. The importance of a good absorbent material is shown in figure 4.8b. Due to the required long exposure time and the defocus the contrast is getting low even when using black velvet. An other effect of the defocus is the massive size increase of the marker. Figures 4.9a and 4.9b both show the marker at a distance of about 40 cm, but image 4.9a is taken with a focus setting of 20 cm, while image 4.9b represents a focus setting of 40 cm. The

Figure 4.7.: Two images of the passive target setup with the LED board illumination on.

marker in the image with the focus setting of 20 cm is strongly defocused and the marker, therefore, significantly larger.

(a) 2586 μs (b) 64867 μs (c) 2391 μs

(d) 2586 μs (e) 48000 μs (f) 24123 μs

Figure 4.8.: Example images of the passive target, used for center extraction. The three images in the first row are captured with a focus setting of 10 cm. The three images in the second row are taken with a focus setting of 50 cm. The subcaptions show the exposure times which were used to take the images.

Two results for an extracted center, an example of a marker in focus and a defocused marker, can be seen in figure 4.9. Because the defocus effect is consistent in all directions, the center extraction works really well and,

therefore, focused and defocused markers are valid results and hence the found point correspondences can be used for further processing.

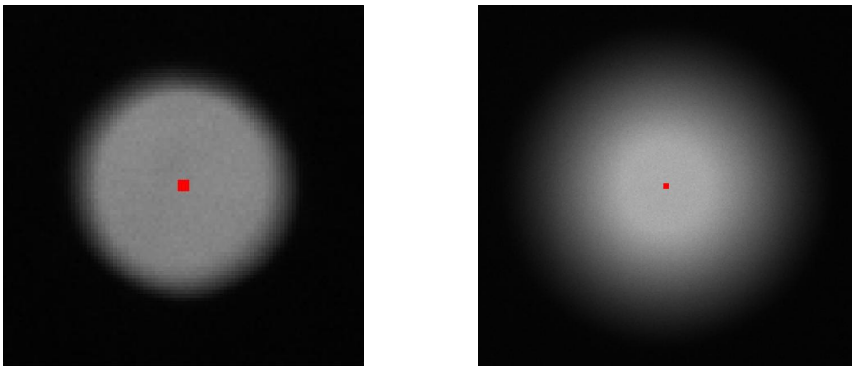

(a) Marker diameter ∼55 pixels (b) Marker diameter ∼100 pixels

Figure 4.9.: Examples of extracted centers, using two images of the passive target for a focus distance of 40 cm. Image 4.9a is in focus but in image 4.9b the target is in distance of about 20 cm to the camera and, therefore, already strongly defocused. The result is a blurred circle which is considerable larger and has no sharp boundaries. The difference in size can be identified by the different resolution (in the left image individual pixels can be already identified).

4.2.2. Active targets

In contrast to the passive target an active target, uses no external illumination. The light source is part of the target or marker itself. To my knowledge, there are no well documented approaches for such active targets besides the usage of displays, which is a completely different category. The method I developed builds on LEDs as light source which are routed into an standard multi mode optical fiber. The other end of the fiber is placed in a mounting which is attached to the coordinate measurement machine.

The setup of the active target can be seen in figure 4.10. The LEDs are soldered onto a printed circuit board which is placed in a box. All LEDs have resistors preceding for current restriction which are dimensioned for the LEDs to have a similar intensity. To neutralize directional influence due to the offset of the LED positions, a diffusing screen is added in front of

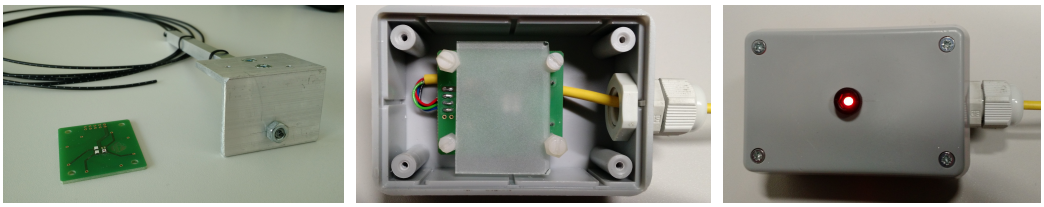

(a) (b) (c)

Figure 4.10.: Device for the active target approach. Image 4.10a shows the printed circuit board with LEDs and fiber optic with mounting device. In image 4.10b the printed circuit board is already connected and fitted with the appropriate resistors for each LED color. The diffusing screen in front of the LEDs reduces all directional effects. Image 4.10c shows the activated device without the fiber optic attached.

the LEDs. In the front of the box a lead-in for the fiber is incorporated. The attached mounting can be seen in figure 4.11 with LEDs activated and deactivated.

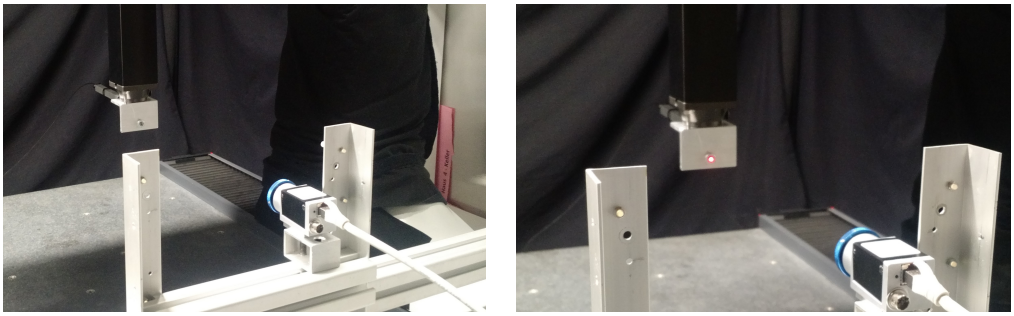

Figure 4.11.: The active target mount fixed to the coordinate measurement machine in off and on condition.

A difference to the passive target can be seen in figure 4.12. If the focus point is in front the target, no simple blur effect occurs but an effect known as bokeh. The image of the light source inherits the form of the aperture and lens impurities and aberrations are visible. But as long as the aperture has a rotation symmetric shape, the result of the centroid calculation is still correct.

Six examples of resulting images to obtain point correspondences using an active target are shown in figure 4.13. The examples are selected to

Figure 4.12.: The observed bokeh effect using a focus distance much closer than the distance of the light source. The left image is taken with the Basler camera with fixed aperture lens. The right image shows an image of the same light source taken with a single lens reflex camera with a flexible aperture (7 blades). The shape is given by the aperture. The circle like artifacts inside are a consequence of aberrations and impurities of the lens.

match the positions of the passive marker examples in figure 4.8. Several distinctive differences can be observed. Due to the small diameter of the optical fiber the marker size is much smaller but the lack of otherwise illuminated objects makes identification easier. As a difference to the passive target, the contrast from marker to background is never an issue and even at the maximum working distance of 70 cm, the exposure time never needs to be higher then 10000 μs, opposed to the 70000 μs observed for the passive target method. The overall difference of the intensities between markers at different distances is also reduced. Even with the decreased exposure time the visibility and homogeneity of the marker is better and, therefore, the threshold operation is easier. Because there are no other illuminated objects, there is no risk of a false identification, but a check for a complete marker is still required. Another problem can occur if the exposure time is too long. Overexposure can lead to sun like rays from the fiber (light source), which impedes the centroid calculation. But overall the handling of the active target setup is significantly easier than the handling of the passive target setup.

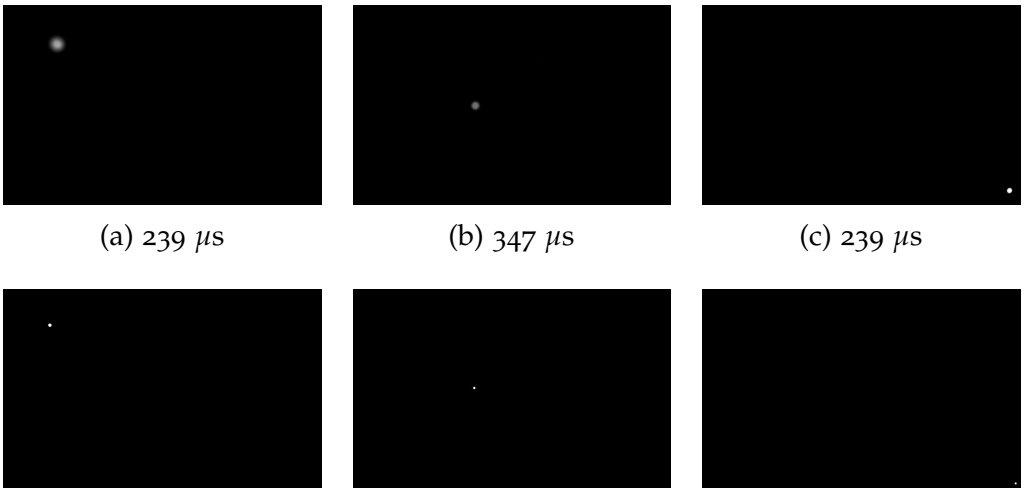

(a) 239 μs (b) 347 μs (c) 239 μs

(d) 1574 μs (e) 8057 μs (f) 5194 μs

Figure 4.13.: Example images of the active target, used for center extraction. The three images in the first row are captured with a focus setting of 10 cm. The three images in the second row are taken with a focus setting of 50 cm. The subcaptions show the exposure times which were used to take the images. (Compare figure 4.8 for significantly higher exposure time required for passive targets.)

4.2.3. Simulation

To acquire a measurement for one setting using the large point cloud (truncated pyramid), an acquisition time of about 80 minutes is necessary. Even using the point cloud with the reduced point number (three layer approach), the time to take a measurement for one setting is about 20 minutes. This leads to the necessity for an alternative, faster approach to to test other setups. The simulation is a well fitting approach because it is possible to create usable data of a point cloud in a couple of seconds. After the point cloud is generated and the position and field of view of the camera are specified, the correction of the parameters is calculated the same way as for the data obtained by measurements using the CMM. Therefore, the calculation of the reprojection can be done the same way and the results can be compared to real data. These results can be used to estimate the viability of an approach or the influence of inaccuracies, e.g. a systematic error due to a poorer produced target or an inaccurate marker localization. Additionally,

it is possible to simulate targets using multiple markers opposed to the approach with the CMM in my methods, where always a single marker is used. Figure 4.4 shows a three layer approach as an example. The purpose of the point cloud in the given simulation was to find the necessary parameters and limits for a feasible planar target.

The first step for the simulation needs the appropriate projection matrix $\mathbf{P}$. This is obtained from the calibration data belonging to the specified setting. The matrix can be rebuilt using the rotation matrix $\mathbf{R}$,the camera matrix $\mathbf{K}$ and the camera position $-\tilde{\mathbf{C}}$ (equation 2.3) or directly be saved and used from the calibration process. The second step is to generate the desired optimal point cloud and optionally to add intentional deviations to simulate the desired error. After that, the points can be projected into the image using $\mathbf{x} = \mathbf{P} \cdot \mathbf{X}$ and lens distortion can be added. Figure 4.14 shows the example of the point could and the projection of the points into the image.

It is important to mention that the method for the lens distortion correction is not designed to be used for arbitrary points. If the coefficients have different signs they neutralize each other and as a result coordinates from outside the image borders are projected into the image. These points are usually significantly outside the image border but if a large 2D target is simulated, this effect already occurs. Therefore, it is important to restrict the approach to points in the field of view or at least close to it. At last, if intended, inaccuracies/errors from the centroid acquisition can be added to the image point. This intentional inclusion of a specified problem allows a very clear evaluation of the impact on the result. After these steps are finished, this gives a set of point correspondences which can be used to calculate a new set of parameters. The last step is to evaluate the result. This is done by calculating the reprojection error (equation 2.11) using the ground truth data (point cloud of the original) and comparing the result to the extracted centers.

4.2.4. Interpolation

Traditionally, a camera calibration and aberration correction is done and used for a very specific focus, aperture and focal length camera setting. If a

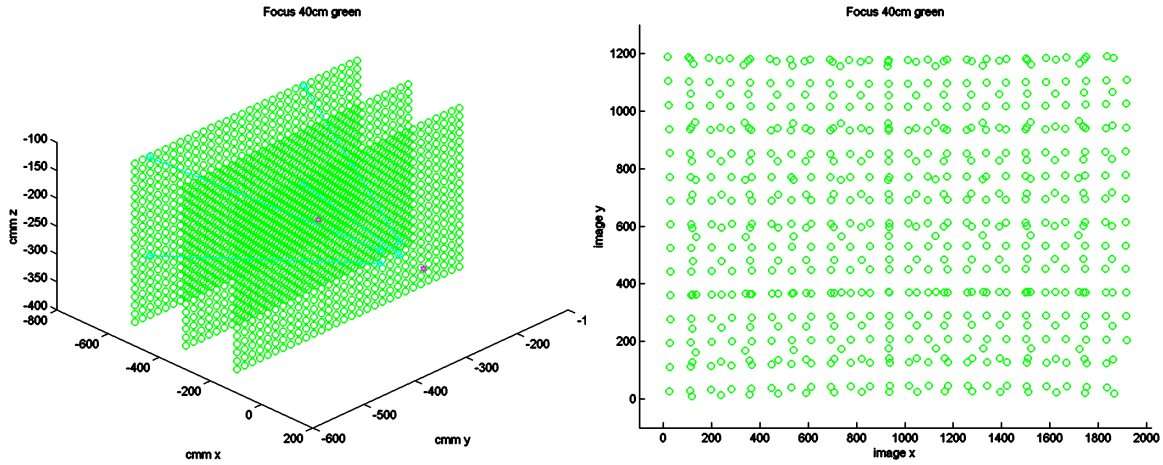

(a) 3D point cloud (b) Projection into the image.

Figure 4.14.: Example of the simulation for a three layer planar target approach. The green circles mark the position of a simulated marker. Figure 4.14a shows the 3D point cloud. The violet stars mark camera and focus point. The allocation of the markers in the image using a known camera position and field of view can be seen in figure 4.14b.

couple of different settings are needed, the number of necessary calibrations and, therefore, measurements grows very fast because a change of focus and aperture (as would the change of focal length of a zoom lens) settings have impact on the resulting parameters. Therefore, the approach to obtain a parameter set for each setting is not feasible. To enable the use of all possible settings despite this constraint, the strategy is to take measurements at specified settings and use them as sample points for an interpolation.

Because of the boundary condition that the parameter interpolation has to be done immediately after a setting changes, the interpolation methods chosen are focused on fast processing time. That said, other, more sophisticated methods may increase accuracy. Two different interpolation methods are used: the focal length is interpolated by the hyperbola function seen in equation 4.6 and all other parameters by linear interpolation (equation 4.7). The calculation of the required coefficients for the linear interpolation is done using linear regression. See figure 4.15 for interpolation examples. If it is necessary to fit specific areas better or to make use of a large number of

interpolation points, the interpolation is also done piece wise. I only considered interpolations for the change of a single setting, because each setting discussed (focus, aperture, color for monochromatic illumination or zoom for a zoom lens) will add a dimension (n in equation 4.8) and, therefore, increase the number of sample points required to interpolate and verify the results massively. Considering the used $m = 7$ sample (measurement) points to determine the parameters for a focus or aperture setting, even an only two dimensional ($n = 2$) approach will require $7^2 = 49$ measurements, with each measurement using a full set of point correspondences. That said, the method by itself should be valid for a multidimensional approach.

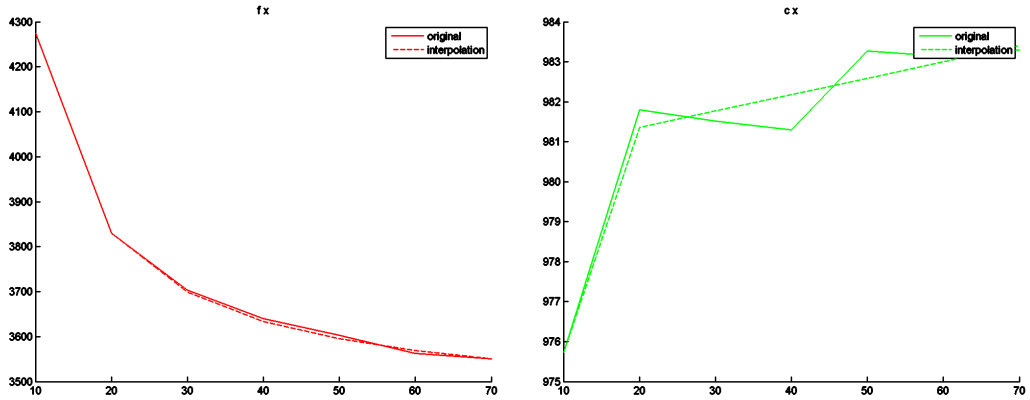

(a) Focal length f_x (b) Principal point c_x

Figure 4.15.: Examples of the used interpolation approach. In the left image the the focal length and the interpolation using the hyperbola function can be seen. The right image shows a coordinate of the principal point, which is interpolated using a piece wise linear regression (although only two pieces in the example). The horizontal axis of all plots shows the distance in cm sampled at $m = 7$ measurement points (10, 20, ... 70 cm), the vertical axis the value of the parameter.

$$y = \frac{a}{x} + b \tag{4.6}$$

$$y = b_1 \cdot x + b_0 \tag{4.7}$$

$$y = m^n \tag{4.8}$$

4.3. Chromatic Aberration

By using a monochromatic camera with a single monochromatic illumination, there is no need for a chromatic aberration correction. But it is possible to combine multiple images, each done with a different illumination color (wavelength).

The evaluation of the effect of the color is a special case in the measurement setup because the illumination is an external source and can be added to a measurement series by taking multiple images with multiple illumination settings without the need to change a lens setting. Given that the images taken are of a static scene with red, green and blue illumination, they can be combined to a standard RGB image. To combine such an image an empty RGB image with three layers is created and the monochromatic color images are placed in the corresponding channels. All experiments done used red, green and blue but the approach to combine multiple images can be used for all colors with static scenes. These combined images feature the same problem of all color images regarding the chromatic aberration.

The method chosen to correct the chromatic aberration is the implicit correction approach, where a camera calibration and lens distortion correction for each color is done and afterwards processed.

In [31] this is approach is mentioned to deliver good results and additionally this builds on a radial model and allows the use of the already acquired point correspondence data, which is already required for the monochromatic aberration correction.

Most of the processing steps are similar to the monochromatic approach, therefore, I only state the important differences. At first, a reference color has to be chosen. For this reference color the calculation of the camera calibration and correction is exactly done the way, which is described in the monochromatic approach for camera calibration and lens distortion correction. For the other color channels the difference is that the exterior camera parameters $\tilde{\mathbf{C}}$ are fixed at the position calculated for the reference color.

The intrinsic parameters and the lens distortion parameters are calculated using this fixed camera position, which means the exterior parameters

are fixed at the reference position in the iterative optimization. After that, the calculated parameters can be applied to correct each image of the corresponding color (of course with respect to the lens) and the three results can be combined into an aberration corrected RGB image.

As a side note, I like to state that if the calculated calibration data is used for monochromatic images, which are not of the reference channel, this can slightly influence the result because it is likely that a more accurate solution could be found, if the exterior parameters were included in the optimization.

Regarding the interpolation there is no difference to the monochromatic method.

4.4. Vignetting

Because there are so many reasons for the vignetting effect to occur the goal is a general correction method, which handles the problem as a whole. All these effects have a radial falloff and that there is the additional benefit that a combination with the other correction methods for a faster processing time is possible. This motivates the use of a radial correction model, opposed to a scanline or lookup table approach.

4.4.1. Vignetting approach

To evaluate and correct the vignetting effect, reference images of a homogeneous target with a homogeneous illumination are necessary. The vignetting effect is already clearly visible in tests using white paper and uniformly arranged off the shelf light sources, or even using the overcast sky, as light source. But shadows and disparities in illumination strength impair the result significantly. Therefore, while the use of exterior light sources is possible, it requires a very special illumination setup, which is expensive, so that, for the executed experiments, a different approach is chosen.

Instead to use an exterior light source, I chose to use the high quality of nowadays LCD displays. A close range image of a uniform white area of an LCD display is used to acquire the necessary images, which are used as reference. In figure 4.16 the measurement setup can be seen. In the top of the image a so called Moiré pattern can be identified. This is an interference pattern which is created because the monitor and the camera sensor use discrete pixel elements. The strength and shape of this effect also varies strongly depending on the used lens and is related to its resolution capacity. Because the Moiŕe pattern causes problems with the required reference images a diffusing screen is used to eliminate the effect.

The smallest influence of the vignetting effect is in the center of the vignetting model (which in the optimal case would be in the image center). Hence this area is used to obtain a reference value I_{ref}. This value represents the expected intensity of the whole reference image (without the vignetting effect). While the use of the image center as correction center is possible,

Figure 4.16.: The measurement setup to evaluate the vignetting effect. The diffusing screen is used to to eliminate the Moiré effect which can be identified above the diffusor.

this leads to unsatisfactory results. Experiments have shown that the use of the principal point improves the result significantly. If the principal point is not available, a centroid calculation of the pixel intensities can improve the result, although not as much as the use of the principal point. Because a camera calibration is part of the process of the lens distortion correction, the principal point is already available and, therefore, used as correction center. A single pixel is very prone to noise. To reduce this influence a mean calculation of several pixels around the correction center is used to calculate the reference value. For my experiments, an average intensity of 7×7 pixels is used to obtain this reference value I_{ref}. The next step is to use a grid pattern to obtain the intensities I_1 to I_n, from all other areas of the image, to

obtain N intensities.

Equation 4.9 represents the correction using three terms for a single pixel with intensity I at distance r from the center.

$$I_{cor} = (1 + \alpha_1 \cdot r^2 + \alpha_2 \cdot r^4 + \alpha_3 \cdot r^6) \cdot I \tag{4.9}$$

To obtain the desired reference value after the correction process, I_{cor} is replaced by I_{ref}. Rearranged, this leads to equation 4.10.

$$\alpha_1 \cdot r^2 \cdot I + \alpha_2 \cdot r^4 \cdot I + \alpha_3 \cdot r^6 \cdot I = I_{ref} - I \tag{4.10}$$

Using the obtained pixel intensities, this can be used to build an overdetermined equation system of the form $\mathbf{A}\boldsymbol{\alpha} = \mathbf{b}$ which can be seen in 4.11.

$$\begin{bmatrix} r^2 \cdot I_1 & r^4 \cdot I_1 & r^6 \cdot I_1 \\ r^2 \cdot I_2 & r^4 \cdot I_2 & r^6 \cdot I_2 \\ \vdots & \vdots & \vdots \\ r^2 \cdot I_n & r^4 \cdot I_n & r^6 \cdot I_n \end{bmatrix} \cdot \begin{bmatrix} \alpha_1 \\ \alpha_2 \\ \alpha_3 \end{bmatrix} = \begin{bmatrix} I_{ref} - I_1 \\ I_{ref} - I_2 \\ \vdots \\ I_{ref} - I_n \end{bmatrix} \tag{4.11}$$

This overdetermined equation system can be solved for $\boldsymbol{\alpha}$ by using the least square method (equation 4.12).

$$\boldsymbol{\alpha} = \mathbf{A}^{-1}\mathbf{A}^T\mathbf{A}\mathbf{A}^T\mathbf{b} \tag{4.12}$$

It is very important to normalize the data for these steps to avoid problems due to numerical instabilities [17]. The mean value of r is calculated and normalized to attain an average value of $\sqrt{2}$ (see equation 2.6).

After the calculation of the coefficients $\boldsymbol{\alpha}$ is done, the correction of the image is simply a calculation of the new intensity I_{cor} for each pixel following equation 4.9.

4.4.2. Interpolation

The interpolation of the alpha coefficients is done using a linear interpolation approach (equation 4.15). To obtain these coefficients, linear regression is used. While for the aperture usually the f-number N is the used characteristic variable, for the interpolation the use of the area yields better results. This makes sense because the amount of light is proportional to the size (area) of the aperture. Using the definition of the f-number and rearranging for the diameter D leads to equation 4.13. Because that the used lenses have a circularly shaped aperture the calculation of the area A follows equation 4.14. In figure 4.17, an example of such an interpolation is shown.

$$D = \frac{f}{N} \tag{4.13}$$

$$A = \frac{f^2 \cdot \pi}{4 \cdot N^2} \tag{4.14}$$

$$y = b_1 \cdot x + b_0 \tag{4.15}$$

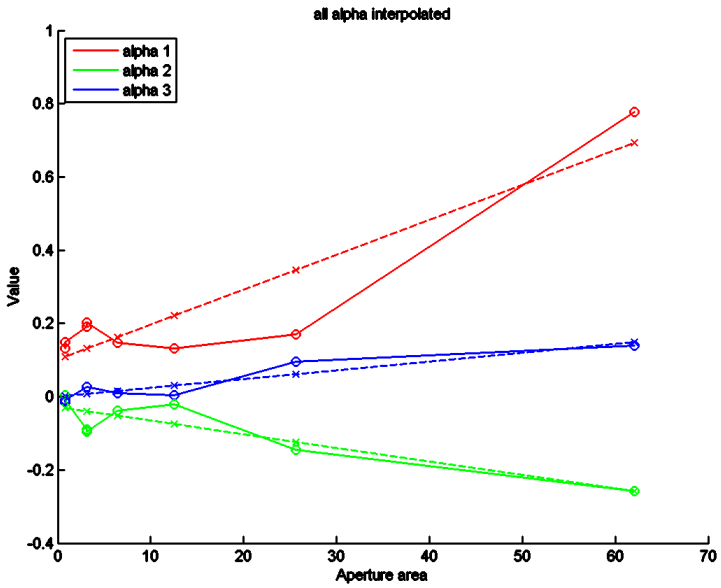

Figure 4.17.: Example plot for a set of alphas found for the correction approach using three terms. The plot shows the result for eight images and the interpolation of this data.

5. Experiments and Validation

This chapter presents extensive experimental validation of the methods presented in chapter 4. The first task is to establish which parameters to use. After that, passive and active target are compared. It is also important to know how the different lens settings of focus and aperture influence the results. Therefore, several experiments using different focus and aperture settings are necessary. At last, the effect of the number of used points and the interpolation is evaluated. Different lenses are used to test the common validity of these results. All experiments are done using a monochromatic camera. An RGB camera would not have any advantage because only monochromatic illumination is used and additional filters, like the Bayer filter, would even decrease the image quality. In total, more than 10.000 images were acquired and processed.

For the experiments a Basler acA 1920 - 48 gm camera (monochromatic with a maximum resolution of 1920×1200 and a value range of 8 Bit), a B&R X-20 CP 1585 control unit, a custom LED board with 4×4 CREE XQE High Density LEDS for red, green and blue, an active target with CREE XQE High Density LEDS for red, green and blue and a couple of different lenses is used. The majority of the experiments is done using the Azure 8 mm S-Mount and the Azure 16 mm S-Mount lenses with a fixed aperture setting of four and the Azure 16 mm C-Mount lens with an aperture setting from 1.8 to 16. All other lenses are only used to acquire isolated samples to validate results. The room used is completely darkened for the time the experiments are performed.

5.1. Camera calibration, distortion and chromatic aberration setup

Figure 5.1 gives an overview of the setup and the interaction between its components. A laptop represents the master where the control for target, camera and illumination is done. The connection to the coordinate measurement machine (CMM) is established via a desktop PC where the instruction file for CMM control with the coordinates of the point cloud is saved. After a position is reached a trigger is sent to the laptop which establishes a TCP connection to the illumination control unit (X-20), which controls the custom LED board and activates the illumination. The laptop triggers the Basler acA 1920-48 gm camera, which takes the image with a resolution of 1920×1200 and sends it to the laptop. This process is done for red, green and blue and repeated for all points in the point cloud.

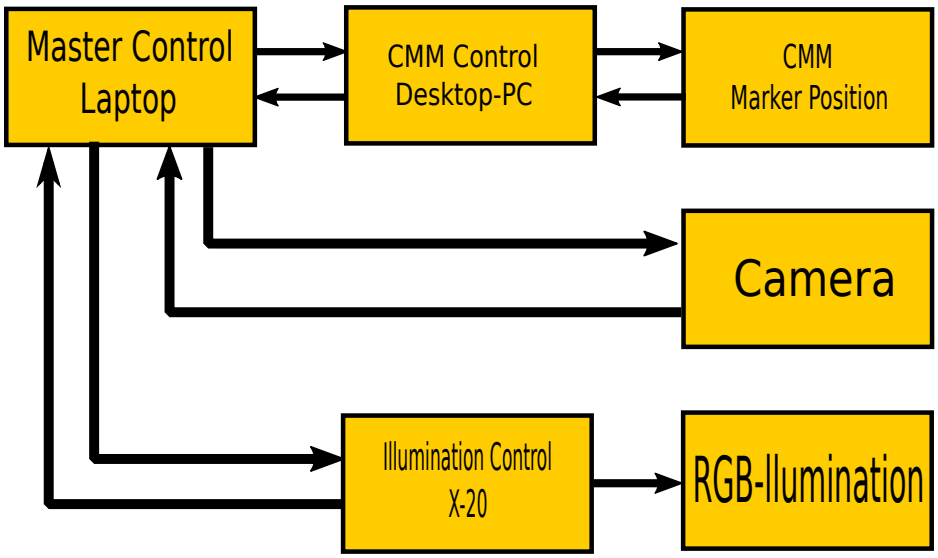

Figure 5.1.: Setup for camera calibration, lens distortion correction and chromatic aberration correction.

In figure 5.2 the procedure for the execution of the method is shown.

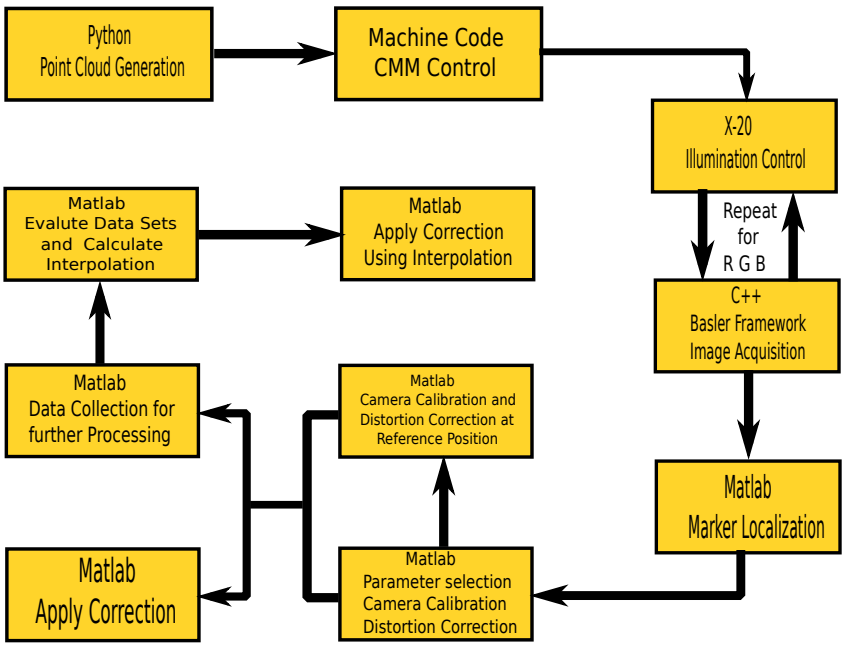

Figure 5.2.: Flowchart of the procedure for lens distortion correction and chromatic aberration correction.

5.2. Focus

It is necessary to validate the chosen methods. Therefore, experiments for all methods are done using different focus settings to establish the constraints for further experiments. These experiments include an evaluation of different parameters, different lenses and active and passive target. For each lens an appropriate point cloud to fit its field of view is generated. This point cloud is used to acquire the necessary point correspondences. A plot of a typical result is shown for every experiment.

The first experiment done is using nine parameters (five linear f_x, f_y, c_x, c_y, s and four non-linear r_1, r_2, t_1, r_2). An Azure 16 mm S-Mount lens is used. The

found parameters and the accuracy of the results, can be seen in figure 5.3. The accuracy is very good but the parameters differ strongly between the different focus settings. This can be explained due to the fact that the results of the tangential parameters and the position of the principal point influence each other significantly in the iterative numerical optimization. Note that this is the only experiment shown, which not only used monochromatic illumination but also white light to verify the approach. Because the results are in line with the expectations, the other experiments are only done for red, green and blue.

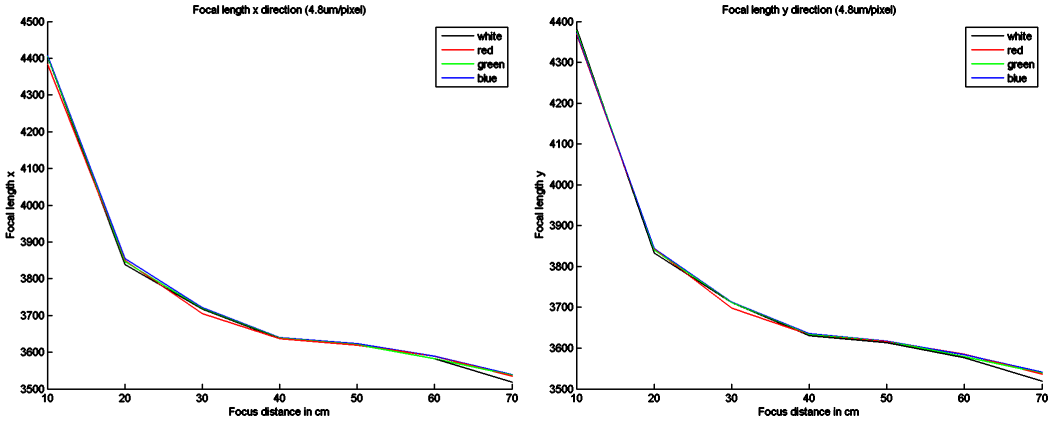

(a) f_x (b) f_y

Figure 5.3.: All parameters Azure S-Mount 16 mm: Horizontal and vertical focal length.

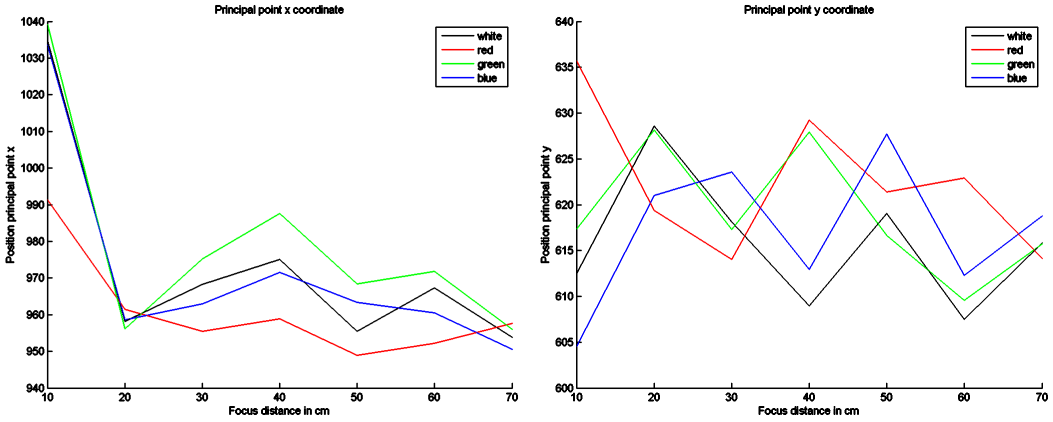

(c) c_x (d) c_y

Figure 5.3.: All parameters Azure S-Mount 16 mm: Principal point coordinates.

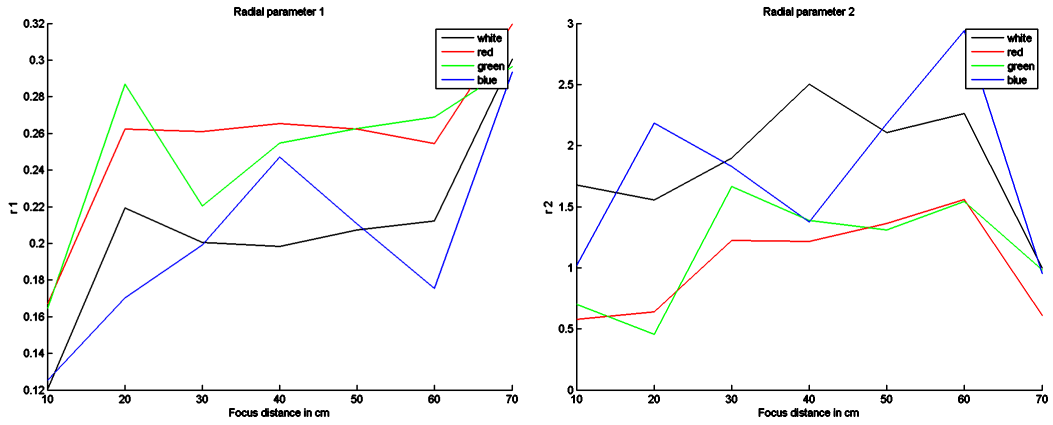

(e) r_1 (f) r_2

Figure 5.3.: All parameters Azure S-Mount 16 mm: Radial parameters.

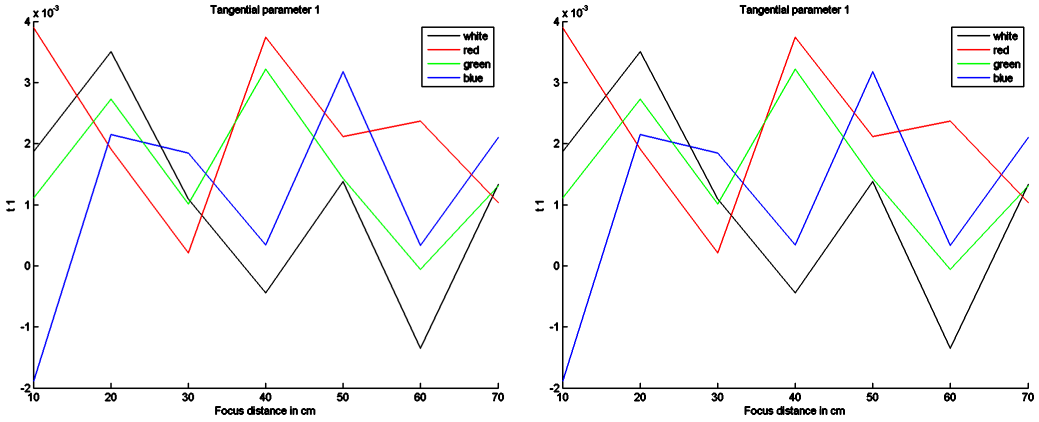

(g) t_1 (h) t_2

Figure 5.3.: All parameters Azure S-Mount 16 mm: Tangential parameters.

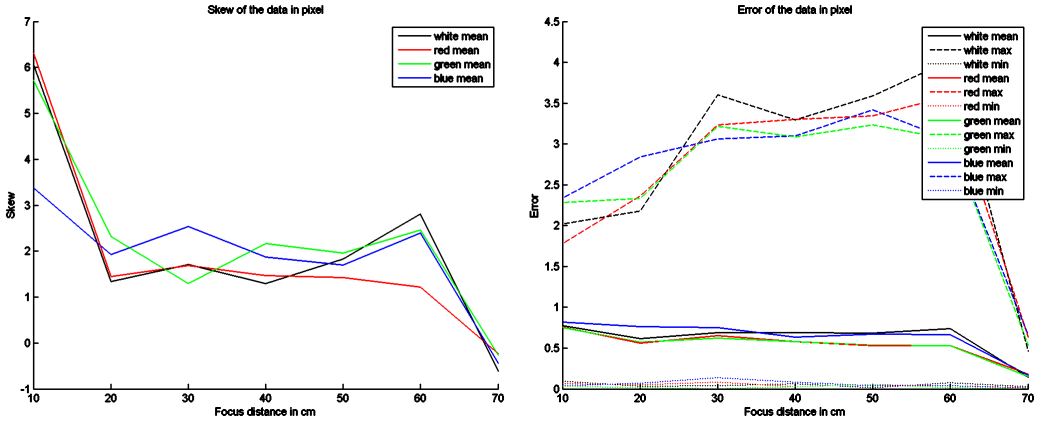

(i) Skew (j) Reprojection error

Figure 5.3.: All parameters Azure S-Mount 16 mm: Skew and reprojection error.

Figure 5.3.: Plots of the results for a calibration using five linear and four nonlinear parameters. The used lens is the Azure S-Mount 16 mm lens. The horizontal axis of the plots shows the focus distance in cm, the vertical axis the value of the parameter.

Because the goal is to have a method which allows to change settings and apply a flexible correction, it is necessary to smooth the behavior of the parameters. A way to accomplish this is to reduce the parameter set. A part of the problem is that principal point and tangential parameters both correct a deviation of the lens from the optimal image center, I made the decision to omit the tangential parameters. This is done because of two reasons: firstly because the correct position of the principal point is important as it is shown in [21], secondly because the tangential parameters are known to create problems in the iterative optimization. The skew is also omitted since it turns out that the effect in regular nowadays cameras is minimal. That said, it is very easy to add the parameters back if a lens/camera can not be modeled without them but at the cost of flexibility.

In the next experiment the exactly same input data is used as for the nine parameter calculation. The accuracy of the results is still very good and can be seen in figure 5.4; the parameters are far less jumpy. Therefore, I made the choice to use only these six parameters in the evaluation of the following experiments.

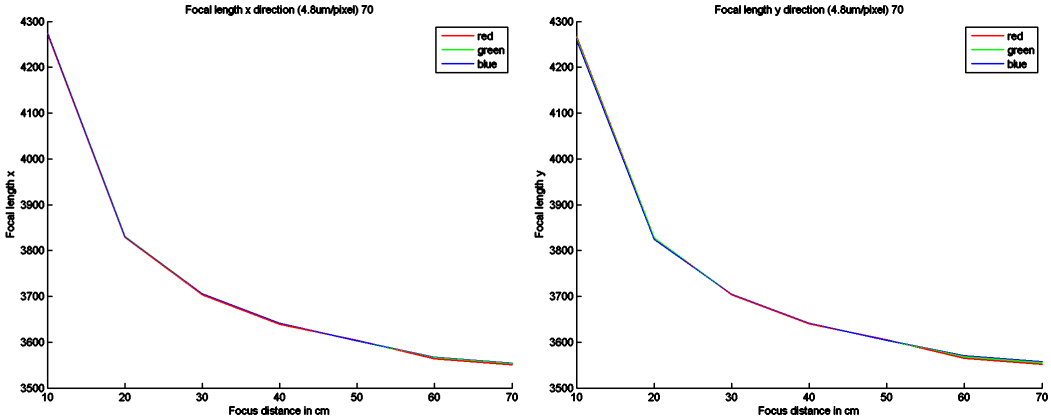

(a) f_x (b) f_y

Figure 5.4.: Radial parameters Azure S-Mount 16 mm: Horizontal and vertical focal length.

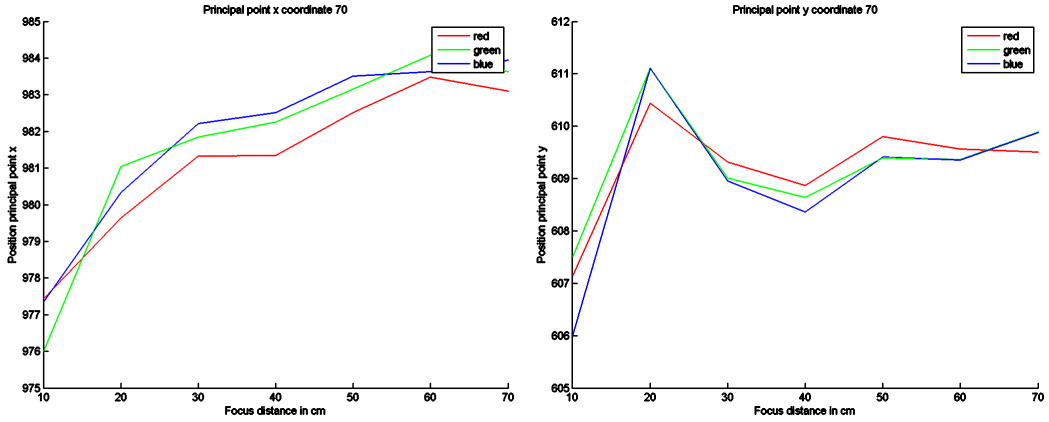

(c) c_x (d) c_y

Figure 5.4.: Radial parameters Azure S-Mount 16 mm: : Principal point coordinates.

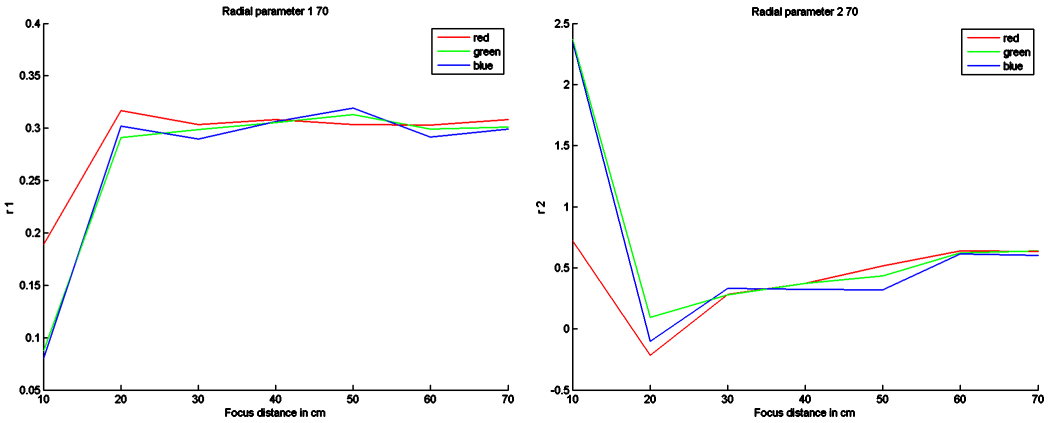

(e) r_1 (f) r_2

Figure 5.4.: Radial parameters Azure S-Mount 16 mm: : Radial parameters.

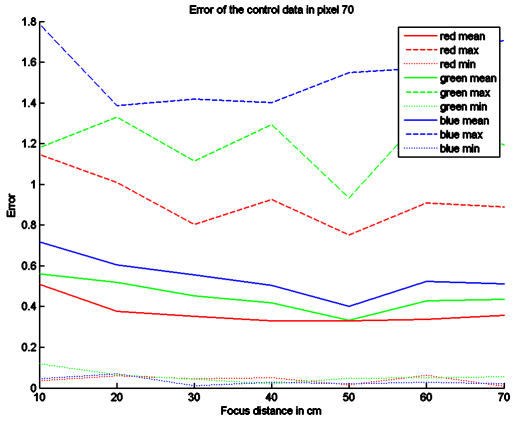

(g) Reprojection error

Figure 5.4.: Radial parameters Azure S-Mount 16 mm: Reprojection error.

Figure 5.4.: Results for the Azure S-Mount 16 mm lens, using four linear and two radial nonlinear parameters (skew and tangential parameters omitted). The horizontal axis of the plots shows the focus distance in cm, the vertical axis the value of the parameter.

The next step is to test if the method can be applied for other lenses. At first, a different focal length is examined. An Azure 8 mm S-Mount lens is used. Because the field of view is much larger, the working distance is reduced to 50 cm, otherwise it would not be possible to include the corners and rims in the point cloud beyond 50 cm because the CMM can not reach these positions. The results, seen in figure 5.5, show that the model fits the shorter focal length and increased field of view nicely, validating applicability of the model.

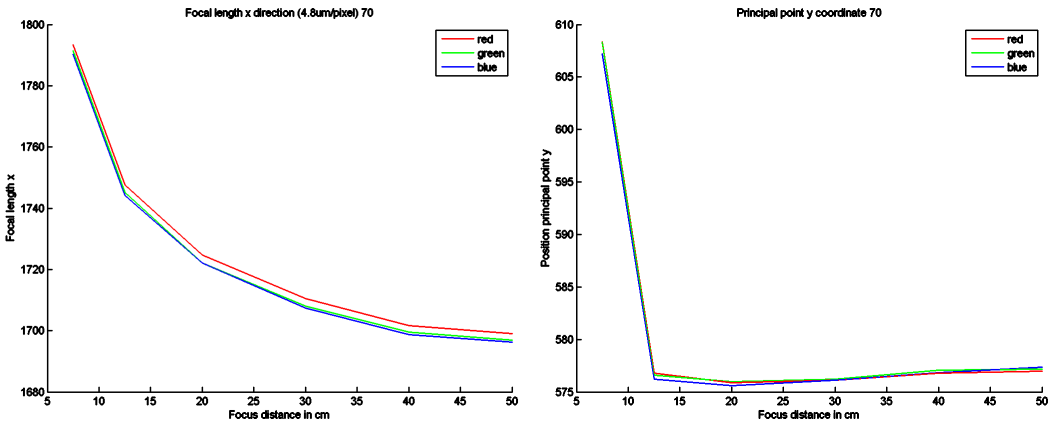

(a) f_x (b) f_y

Figure 5.5.: Radial parameters Azure S-Mount 8 mm: Horizontal and vertical focal length.

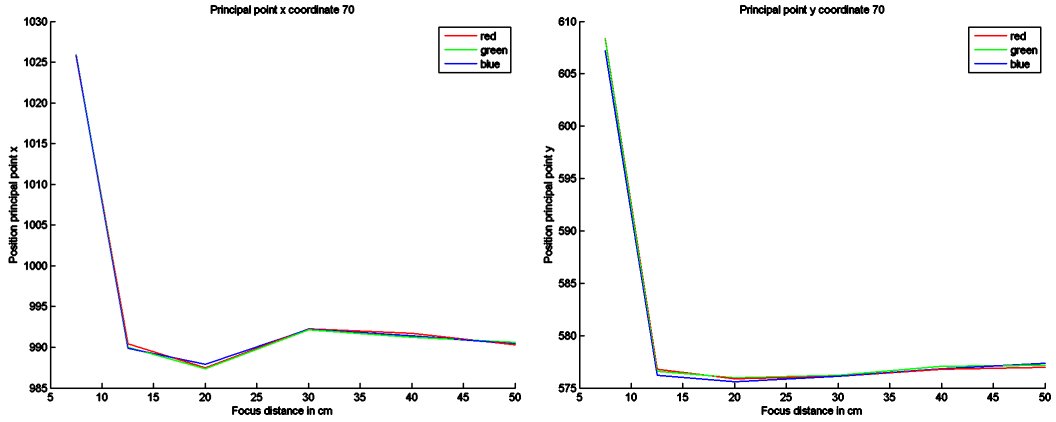

(c) c_x (d) c_y

Figure 5.5.: Radial parameters Azure S-Mount 8 mm: Principal point coordinates.

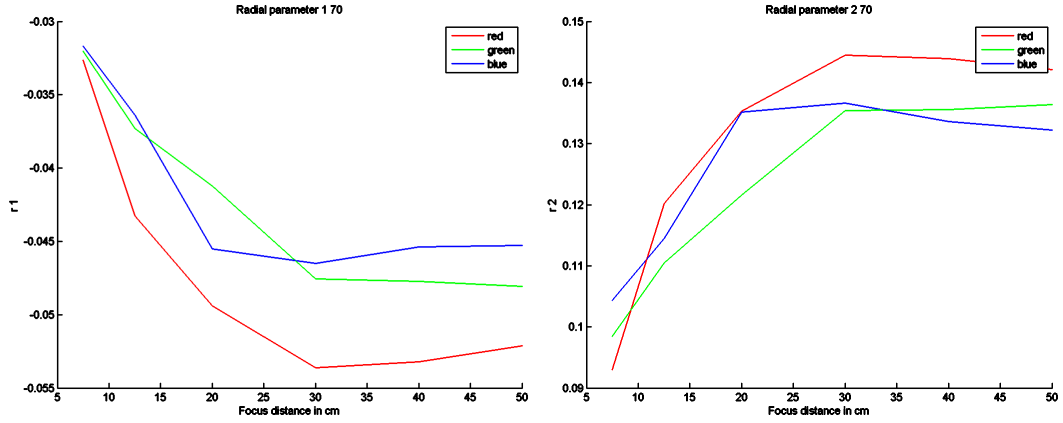

(e) r_1 (f) r_2

Figure 5.5.: Radial parameters Azure S-Mount 8 mm: : Radial parameters.

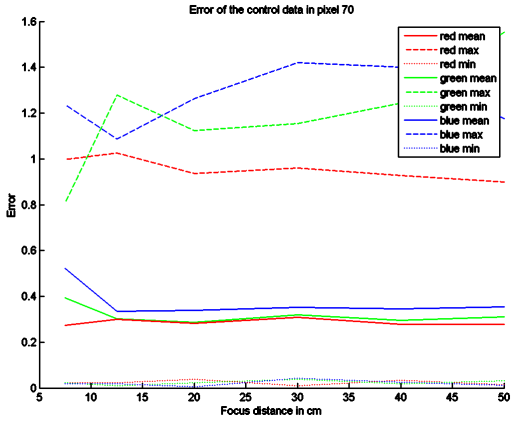

(g) Reprojection error

Figure 5.5.: Radial parameters Azure S-Mount 8 mm: Reprojection error.

Figure 5.5.: Results for the Azure S-Mount 8 mm lens, using an passive target, four linear and two radial nonlinear parameters (skew and tangential parameters omitted). The horizontal axis of the plots shows the focus distance in cm, the vertical axis the value of the parameter.

In figure 5.6 the results for the active target are shown. The used lens is an Azure 16 mm C-Mount lens. Because the previous experiments suggested that quality of the three layer approach is similar to the truncated pyramid the experiments for the active target were only done using the three layer approach for 10 to 50 cm.

To be able to compare the results the experiment was repeated for the passive target using the exactly same point cloud and lens (see 5.7). Due to an error in image acquisition, which I unfortunately recognized too late, the 10 cm results for the passive target had to be omitted but the available distances from 20 to 50 cm show that the results are very similar. This holds true for the parameter values as well as for the accuracy and confirms the applicability of an active target.

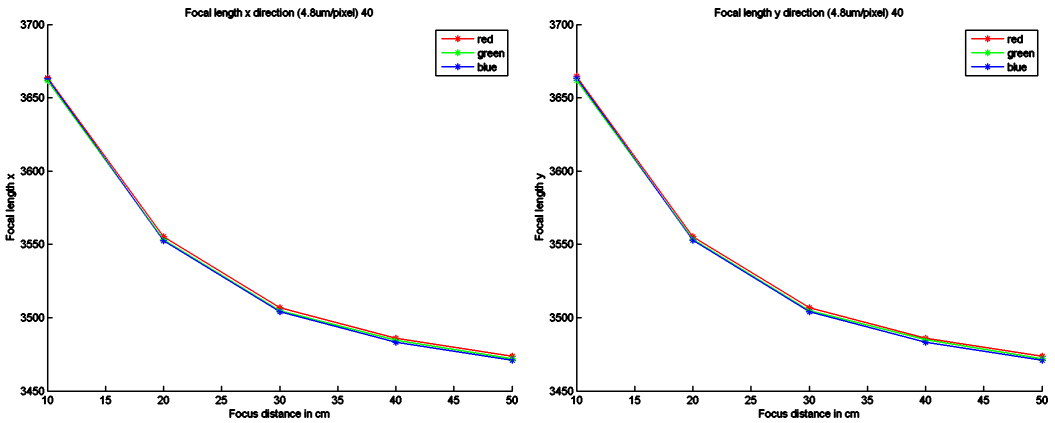

(a) f_x (b) f_y

Figure 5.6.: Active target Azure C-Mount 16 mm: Horizontal and vertical focal length.

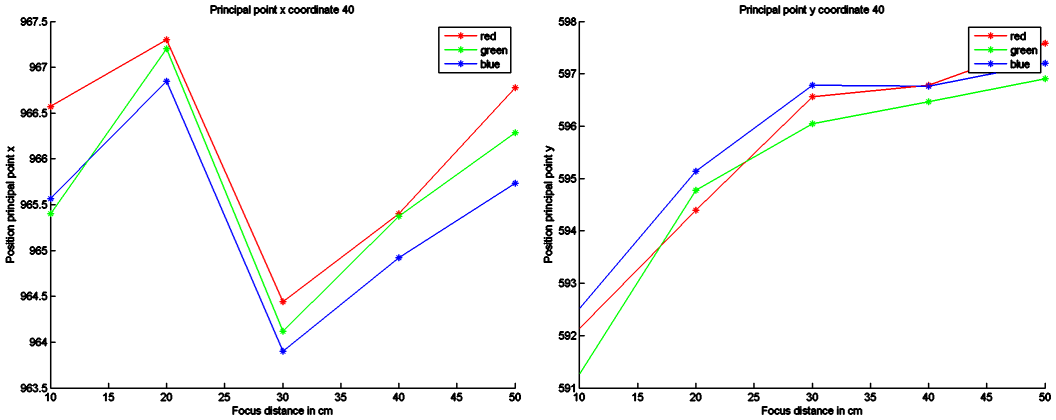

(c) c_x (d) c_y

Figure 5.6.: Active target Azure C-Mount 16 mm: Principal point coordinates.

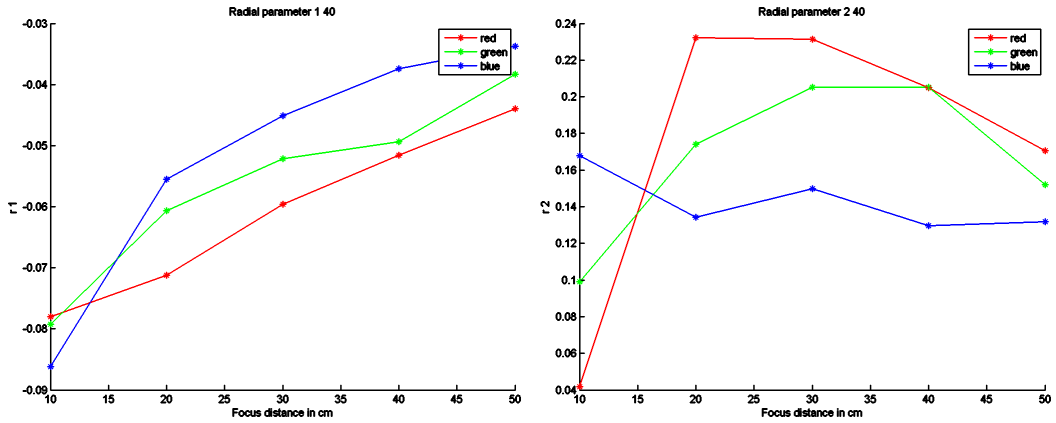

(e) r_1 (f) r_2

Figure 5.6.: Active target Azure C-Mount 16 mm: Radial parameters.

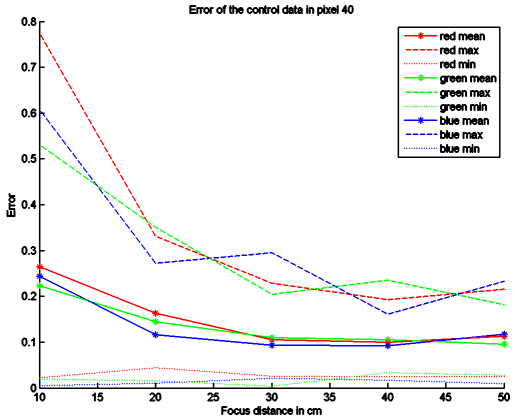

(g) Reprojection error

Figure 5.6.: Active target Azure C-Mount 16 mm: Reprojection error.

Figure 5.6.: Results for the Azure C-Mount 16 mm lens with active target, using four linear and two nonlinear parameters. The horizontal axis of the plots shows the focus distance in cm, the vertical axis the value of the parameter.

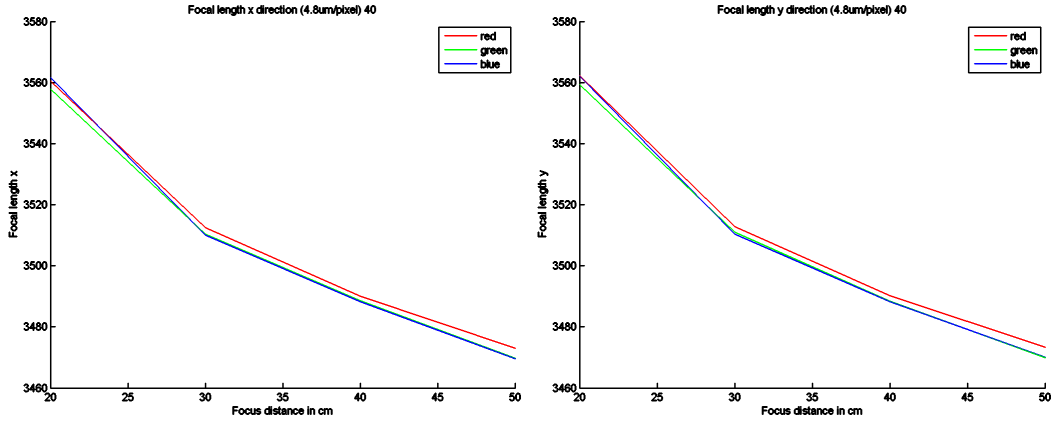

(a) f_x (b) f_y

Figure 5.7.: Passive target Azure C-Mount 16 mm: Horizontal and vertical focal length.

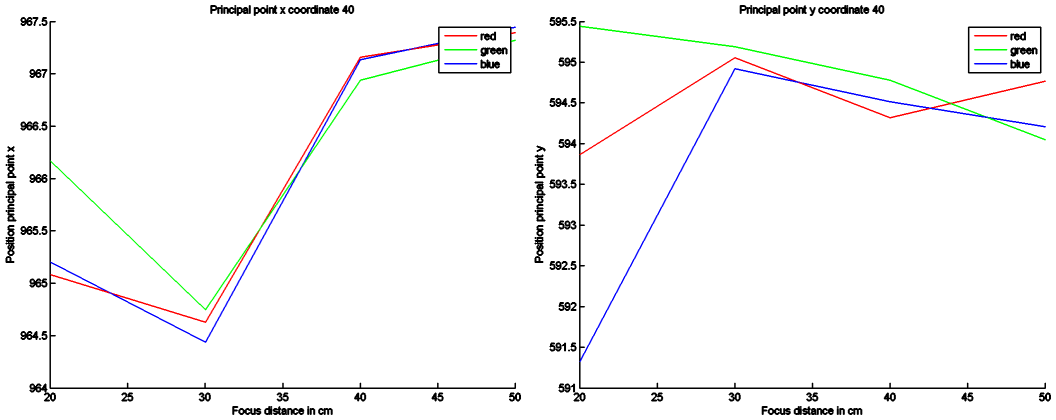

(c) c_x (d) c_y

Figure 5.7.: Passive target Azure C-Mount 16 mm: Principal point coordinates.

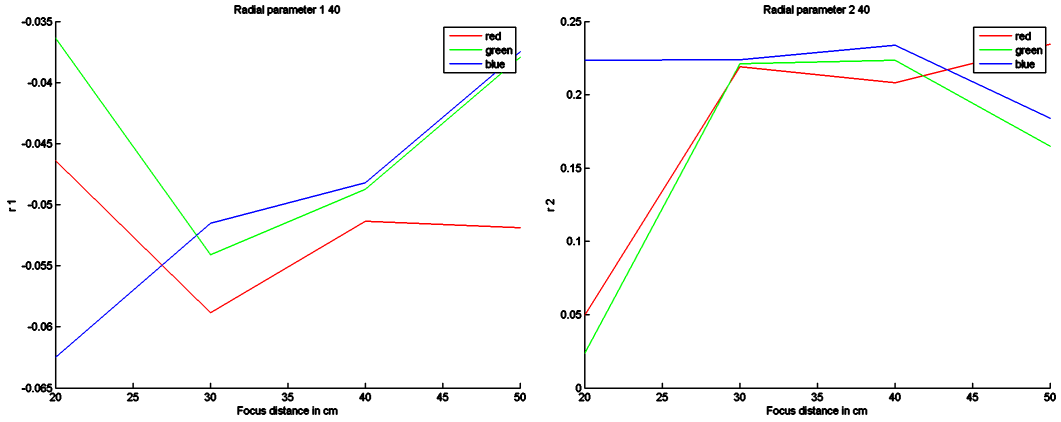

(e) r_1 (f) r_2

Figure 5.7.: Passive target Azure C-Mount 16 mm: Radial parameters.

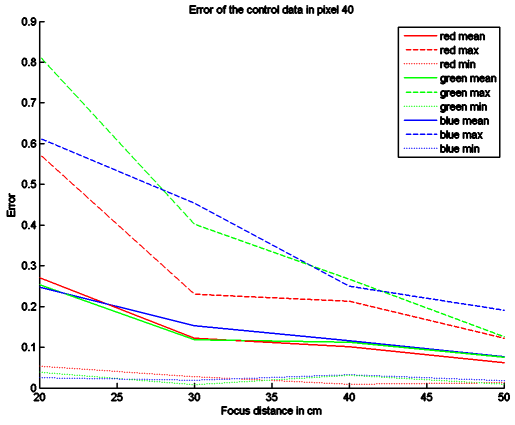

(g) Reprojection error

Figure 5.7.: Passive target Azure C-Mount 16 mm: Reprojection error.

Figure 5.7.: Results for the Azure C-Mount 16 mm lens with passive target, using four linear and two nonlinear parameters. The horizontal axis of the plots shows the focus distance in cm, the vertical axis the value of the parameter.

After obtaining the parameters and calculating the reprojection error an additional practical validation is vital. Using different focus settings, images of a checkerboard are taken to evaluate the results.

The correction has to be calculated for every pixel in the image. It is important to use an inverse mapping method. A forward mapping has two problems. Firstly it would create holes in the result image and secondly there is no analytical solution. Therefore, iterative steps are necessary to calculate the resulting position of a pixel. Using inverse mapping the resulting image can simply be computed pixel by pixel applying the already known lens distortion equations 2.15 and 2.16. To determine the pixel intensities the fast nearest neighbor approach or the more exact bilinear interpolation, seen in equation A.3 is used. Additionally to the equation and a short explanation the graphical interpretation of the bilinear interpolation can be found in appendix A.4. An example of the results can be seen in figure 5.8 (Azure S-Mount 16 mm with a focus setting of 50 cm, passive target). The lines from the checker board in the resulting images are straight but the corrected image has a barrel shape , which results from pincushion lens distortion of the lens. As expected the result using the bilinear interpolation looks much more natural.

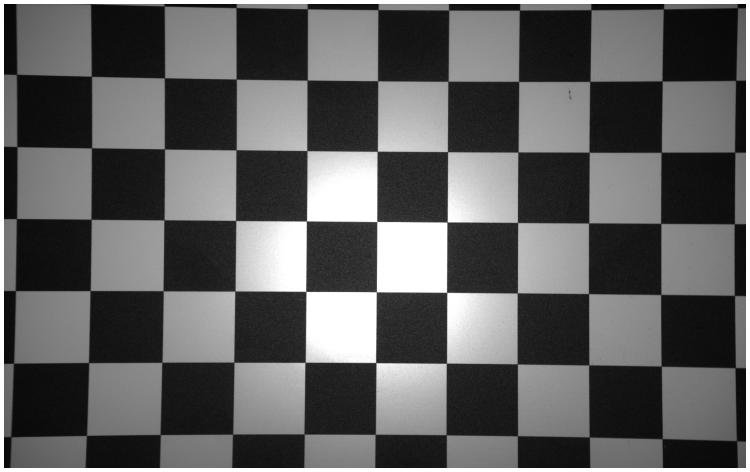

(a) Checkerboard image original.

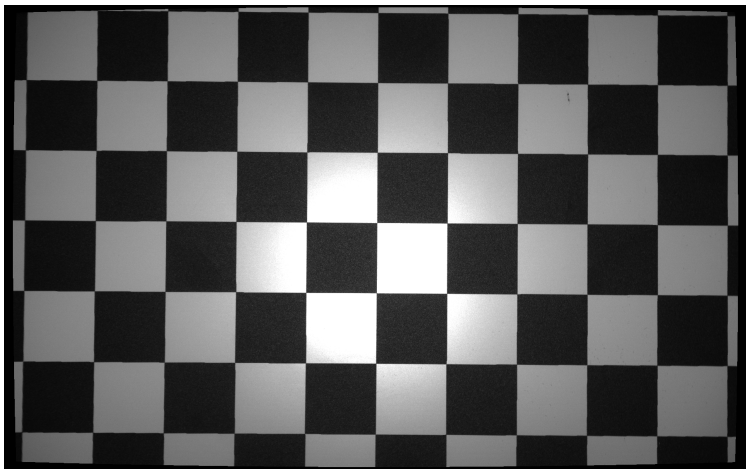

(b) Checkerboard image corrected, nearest neighbor.

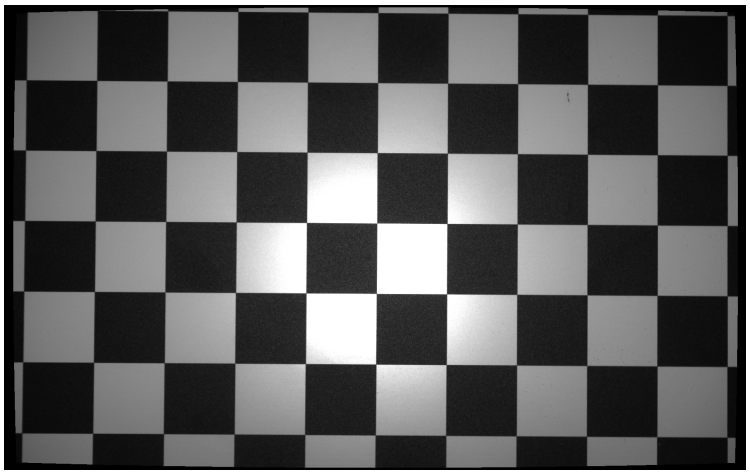

(c) Checkerboard image corrected, bilinear interpolation.

Figure 5.8.: Checkerboard original and corrected images. The method and the parameters used for the correction are identical. The difference is the calculation of pixel intensities. Image 5.8b is done using nearest neighbor algorithm, image 5.8c uses the bilinear interpolation.

In general the experiments yield very good results. This is true for the quantitative analysis of the reprojection error and the qualitative analysis of the corrected images. The evaluation of all performed experiments with changed focus settings shows a clear tendency for the focal length parameters. The trend is always a hyperbola, which allows a clear guideline for processing. The other parameters do not follow such a distinctive behavior but after the omission of the tangential parameters, a trend is visible. All experiments show a divergence of the typical parameter values in the close range of the lens. This suggests that the specified working distance should exclude this close range (only use areas farther away), or that close range measurements only should be used after being handled with a special treatment. A possible solution is to divide the range into more sample points and process the areas piece wise.

The experiments show that both methods, the truncated pyramid and the three layer method, generate good results. Because of the possibility to use a 2D target and the generally faster setup and processing time the three layer approach is favorable in most situations. The comparison of a single active and passive marker leads to very similar results. Therefore, both approaches can be used depending on the purpose. If there is the need for a target, which is easy to fabricate, the passive target is the choice. But the active target is easier to handle in image acquisition and image processing. Therefore, I would recommend the active target if the technical requirements can be met.

If targets using multiple markers are used, the active target provides an important additional advantage. For an active target it is possible to control each marker independently. This enables the option to control exactly which markers are visible in the acquired image, therefore, allowing to use the optimum number and position of points for each image. If the pattern of the active marker elements is fine enough the target can be optimized for every setup. This is impossible for the passive target because the illumination can not be controlled to add or remove markers. Therefore, the result for a target containing multiple markers is clearly in favor of the active target. Compared to the passive target, the active target offers significant benefits, which can be used to design a faster acquisition approach with optimal patterns, for every situation. This advantage can be easily combined with the three plane approach.

5.3. Aperture

The influence of the aperture is the next setting to be evaluated. For that the Azure 16 mm C-Mount lens is used at a fixed focus distance of 30 cm. The experiments are done using the active target and cover the range of f-numbers from 1.8 to 16 using six sampling points, 1.8, 2.8, 4, 5.6, 8 and 16. The results can be seen in figure 5.9.

The use of the aperture area instead of the f-number increases the tangibility and the parameters show a clear trend. All experiments show that the values of the focal length of the camera matrix increase for a larger area (lower f-number). The effect is small compared to the change between different focus settings but considering the effect increases the accuracy. The radial parameters differ strongly which limits the ability to make a definite statement but in respect that a larger r_1 value leads to a smaller r_2 and vice versa, a trend for each color can be seen. Overall the differences between the colors seem to increase slightly the larger the area of the aperture is. This would be consistent with the knowledge that the longitudinal chromatic aberration increases with the diameter of the aperture causing a more blurred image.

The accuracy is good for all results but even better for larger f-numbers (smaller area). This can be explained due to the fact that low f-numbers lead to a small depth of field and, therefore, additionally to the blur from the longitudinal chromatic aberration, the results even get more blurry and it gets more and more difficult to determine the exact marker position.

The influence of the aperture on the correction result is significant enough to conclude that an inclusion of the aperture parameters will increase the overall accuracy of the correction. But the effect is smaller than the effect of the focus and, therefore, it has to be done on top of that, which adds a costly dimension in complexity.

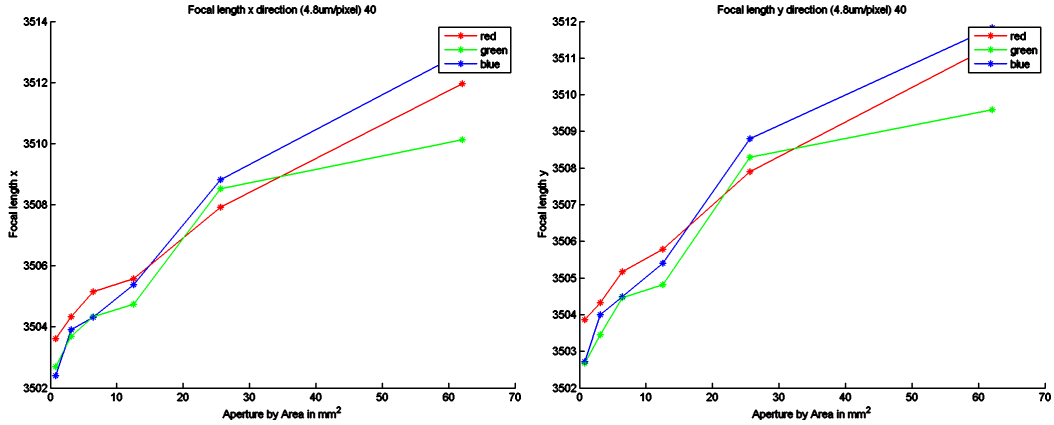

(a) f_x (b) f_y

Figure 5.9.: Aperture Azure C-Mount 16 mm: Horizontal and vertical focal length.

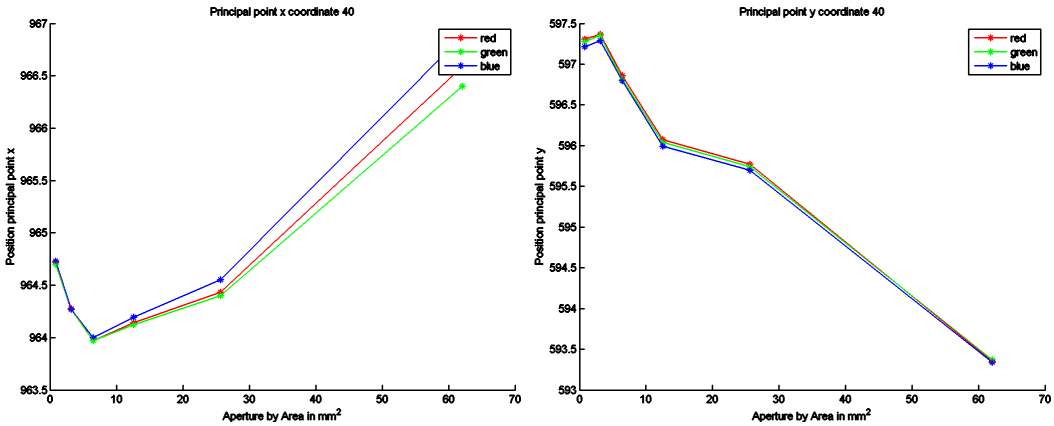

(c) c_x (d) c_y

Figure 5.9.: Aperture Azure C-Mount 16 mm: Principal point coordinates.

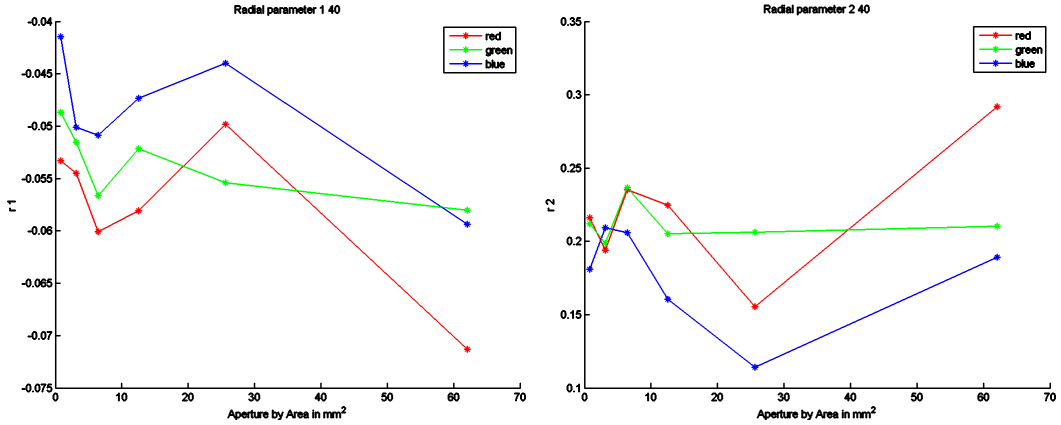

(e) r_1 (f) r_2

Figure 5.9.: Aperture Azure C-Mount 16 mm: Radial parameters.

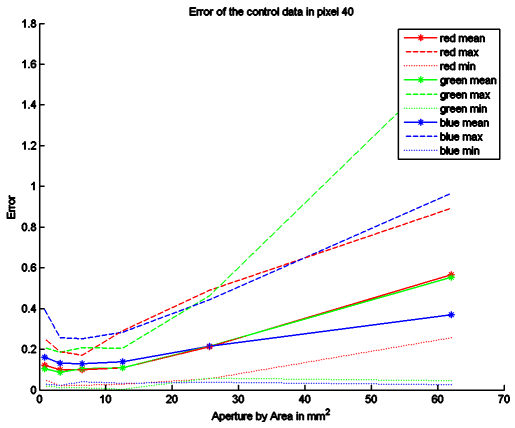

(g) Reprojection error

Figure 5.9.: Aperture Azure C-Mount 16 mm: Reprojection error.

Figure 5.9.: Results for the Azure S-Mount 16 mm lens evaluating the influence of the aperture, using four linear and two nonlinear parameters. The horizontal axis of the plots shows the focus distance in cm, the vertical axis the value of the parameter.

5.4. Number of points

The used point clouds are optimized to cover the whole volume of the field of view of a lens. This leads to excellent results and assures that the results are meaningful. But the acquisition is very time consuming. Therefore, it is worthwhile to know how many point correspondences are necessary to achieve a certain accuracy. A subset of points is chosen from the full set of point correspondences and the correction parameters are calculated by only using this subset. Although it is theoretically possible to calculate the needed projection matrix using only six, equations the minimum number chosen was ten for more stable results. Additionally, the points selected from the point cloud follow a predefined rule for a meaningful result. Different corner points, edge points and grid points are chosen alternately in different planes. This eliminates the strong influence a randomly chosen set can produce and describes the performance a well chosen set produces. The point correspondences which are not in the subset for the calculations are used as validation set to evaluate accuracy. If all points are used, the reprojection error is calculated for all point correspondences.

The results can be seen in figure 5.10. The plots show the mean error for the whole experiment using this particular number of points to calculate the correction. The results show a clear trend for all experiments. Ten point correspondences produce a rather large error but using twenty points already reduces the error significantly. Using thirty and more points the error no longer decreases. This leads to the conclusion that a very good result can be achieved by using thirty well chosen points in three layers. This result lies in the middle of the sixty points used by Tsai [43] and the result of [45], where no improvement could be found beyond eighteen points, but both methods differ significantly to the method I used.

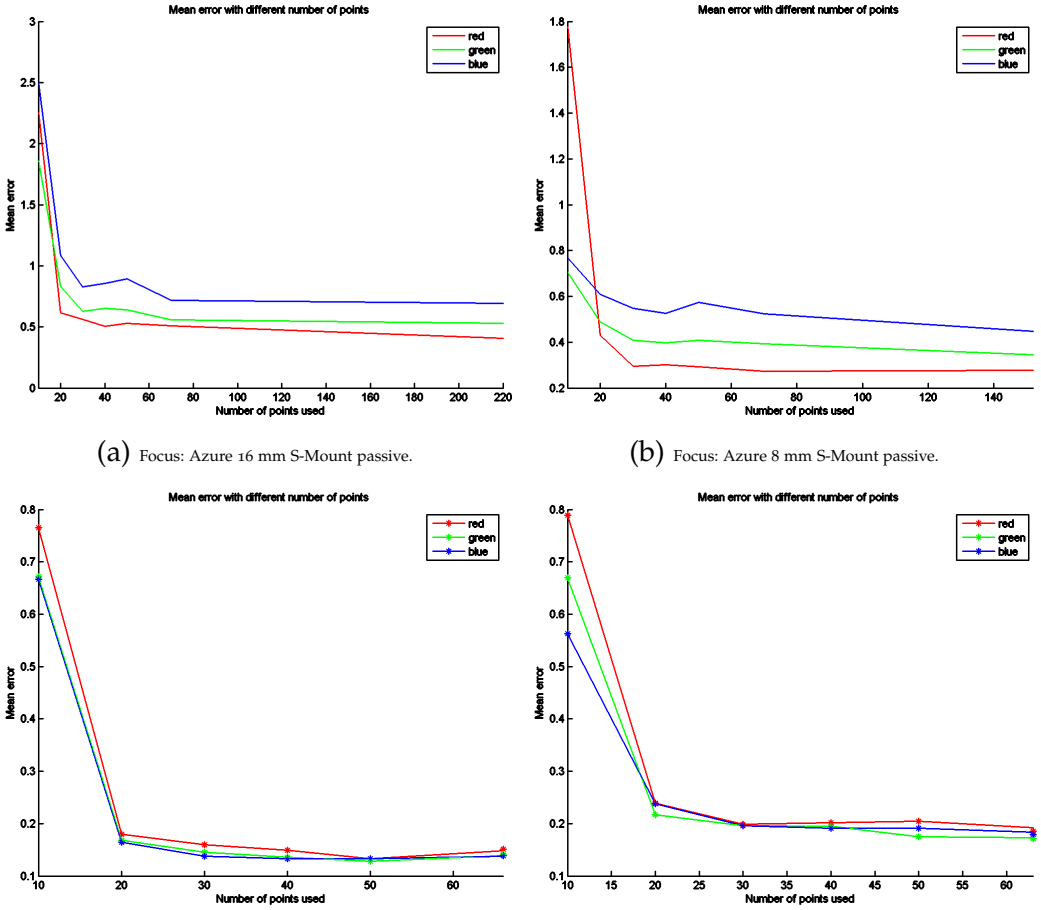

(a) Focus: Azure 16 mm S-Mount passive.

(b) Focus: Azure 8 mm S-Mount passive.

(c) Focus: Azure 16 mm C-Mount active.

(d) Aperture: Azure 16 mm C-Mount active.

Figure 5.10.: Four plots of the mean reprojection error in pixels for a measurement series in dependence of the number of points used to calculate the parameters. Top left plot for the Azure 16 mm S-Mount series. Top right plot for the Azure S-Mount 8 mm series. Bottom left plot using the active target with the Azure C-Mount. Bottom right plot using the aperture evaluation series.

5.5. Simulation

This simulation is used to verify two topics: to evaluate the performance and possible problems of a 2D target with translation and to evaluate the effect of systematic errors and inaccuracies. Tables 5.2 and 5.1 show the reprojection error in pixel for two lenses, the Azure 8 mm and 16 mm S-Mount, in regard of the focus setting experiments. Because the data is too comprehensive too show every single result, the minimum, maximum and mean values of the partial results are taken and the mean value of all focus distances is calculated.

At first the effect of the usage of a 2D target is evaluated. This was already done before the second point cloud method (three layers) was realized and the cornerstone for the design. The ground truth data is using the point cloud method one (with the truncated pyramid). The simulation results for a calibration and correction using the usual six parameters (f_x, f_y, c_x, c_y, r_1 and r_2) can be seen in the first rows of tables 5.1 and 5.2. The results achieve the expected accuracy and are verified in the practical realization of method two. A surprise is the fact that even points beyond the three layers are accurate if the three layers are chosen as proposed (figure 4.4). The second rows show the impact of a model without nonlinear parameters. The error increases dramatically showing the importance of the nonlinear parameters and optimization. The third row shows the result if only single calibration is done at 30 cm and used for all focus distances. The error gets tremendous even though for 30 cm the results are naturally as good as in row one. All simulated values correspond nicely with the results achieved with later executed measurements using this three layer approach.

The other rows in the table correspond to the evaluation of induced errors. All results are acquired using the specified six parameters. The simulations show that already small systematic errors, like a tilt of 0.1° (which leads to a maximum deviation of 1 mm at the larger target (100 × 62 cm)) or a small offset (which is always implied in all directions and would correspond to a measurement error of the coordinates) increases the reprojection error significantly. The last rows show a combination of deviations in which the reprojection error stays under one pixel, which can be seen as realistic requirement.

As a conclusion it can be said that the accuracy requirements for a good calibration target are very rigid. The simulations for the two lenses suggest that to stay within a reprojection error limit of under one pixel the requirements could be as following: The 2D target is allowed to be tilted in a way that the coordinate difference from the start to the end of the field of view can be about 250 μm additionally to an allowed systematic offset of about 20 μm in all directions. The last requirement would be that a marker can be located with an accuracy of ± 0.1 pixel.

	mean			min			max		
	r	g	b	r	g	b	r	g	b
Optimal setup	0.32	0.39	0.49	0.001	0.001	0.01	1.14	1.38	1.79
No nonlinear parameters	6.98	6.75	6.75	0.07	0.02	0.08	37.05	36.69	36.21
One single calibration for all distances	34.264	34.72	34.69	1.06	1.25	1.17	149.60	147.65	149.63
Tilt 0.1° (max 600 μm)	1.35	1.36	1.36	0.06	0.07	0.04	5.66	5.70	5.75
Tilt 0.05° (max 300 μm)	0.61	0.64	0.71	0.03	0.01	0.02	2.79	3.17	3.41
Offset 100 μm	1.90	1.93	1.92	0.16	0.21	0.24	6.00	6.29	6.27
Offset 20 μm	0.47	0.51	0.57	0.02	0.01	0.01	1.75	2.00	2.23
Tilt 0.05° (max 300 μm) offset 20 μm ± 0.1 pixel	0.75	0.77	0.81	0.02	0.04	0.01	3.26	3.78	3.85

Table 5.1.: Simulation results of the reprojection error in pixel for an Azure 16 mm S-Mount lens in various situations and induced errors for target and acquisition. The simulation uses a planar target of 35×30 cm in three layers. The shown results are mean values of the partial results of all used distances.

	mean			min			max		
	r	g	b	r	g	b	r	g	b
Optimal setup	0.26	0.29	0.33	0.01	0.02	0.02	1.11	1.08	1.34
No nonlinear parameters	2.06	1.69	1.53	0.09	0.09	0.07	4.40	3.39	6.35
One single calibration for all distances	43.95	43.78	43.73	19.50	20.31	20.89	104.56	105.42	105.81
Tilt 0.1° (max 1 mm) offset 20 μm ± 0.1 pixel	3.50	3.45	3.49	0.15	0.24	0.21	15.86	15.82	16.18
Tilt 0.015° (max 300 μm) offset 20 μm ± 0.1 pixel	0.84	0.85	0.87	0.01	0.02	0.03	3.68	3.79	4.06

Table 5.2.: Simulation results of the reprojection error in pixel for an Azure 8 mm S-Mount lens in various situations and induced errors of target and acquisition. The simulation uses a planar target of 100×62 cm in three layers. The shown results are mean values of the partial results of all used distances.

5.6. Interpolation

The evaluation of the quality of the interpolation is shown for data obtained by measurements with the CMM and data generated in the simulation. All interpolations done use the same approach. The first sample point is excluded from the interpolation because the close range data shows a significantly different behavior. Therefore, it would require a special treatment, but there is no additional data available to verify the results. But in general, a piece wise interpolation, which handles the close range and the area farther away would be a reasonable approach. From the remaining sample points, three are chosen. These points are used to calculate the coefficients of the hyperbola for the focal length and the linear regression coefficients for the other parameters. Using these coefficients, a new parameter set is calculated. This process has to be repeated for each setting or/and lens. The obtained parameter sets are used to calculate the reprojection errors.

At first, the results for interpolation of the CMM measurement data are shown. Figure 5.11 shows the reprojection error for the interpolation of the CMM measurements of the Azure 16 mm S-Mount lens. While the mean error for the CMM measurement data follows a relatively straight line at an error range of below one pixel, the interpolation shows a peak, where the reprojection error increases significantly, but even there the mean error stays below two pixel. Figure 5.12 compares measurement and interpolation data for the Azure 8 mm S-Mount lens. The shape of the results of the reprojection is similar to the results of the Azure 16 mm S-Mount lens but the difference of measured and interpolated reprojection error is larger. The mean reprojection error goes up from below 0.5 pixel for the measurement data to up to 2.5 pixel at the peak for the interpolation data.

The second set of experiments is using the data generated in the simulation. The simulation data chosen are the data sets, which are tailored to have their mean reprojection error under one pixel (corresponding to tables 5.2 and 5.1 , last row). The reprojection error for the used simulation data and the interpolation of this simulation data is shown in figures 5.13 and 5.14. The behavior is very similar to the CMM measurement data and its interpolation, which confirms interpolation and simulation results. The

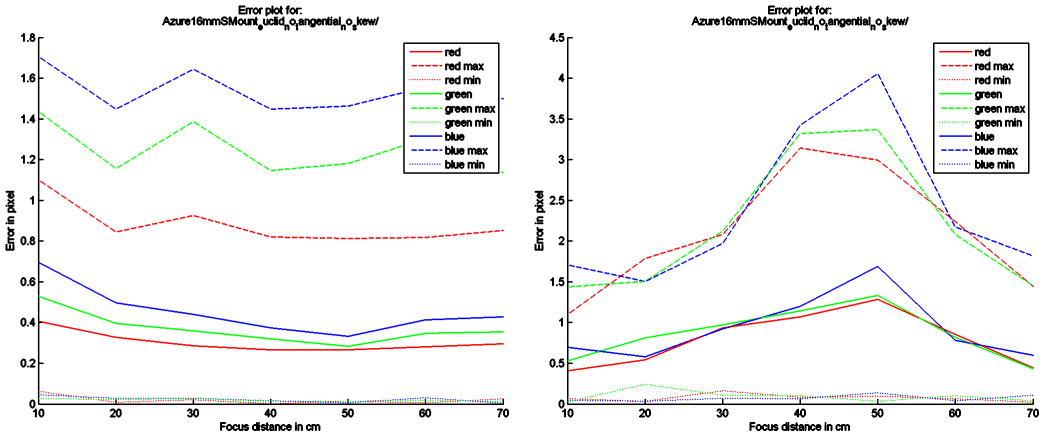

(a) CMM Measurement (b) Interpolation

Figure 5.11.: Mean error in pixel using the data of the CMM measurements for the Azure 16 mm S-Mount and the interpolation for the data.

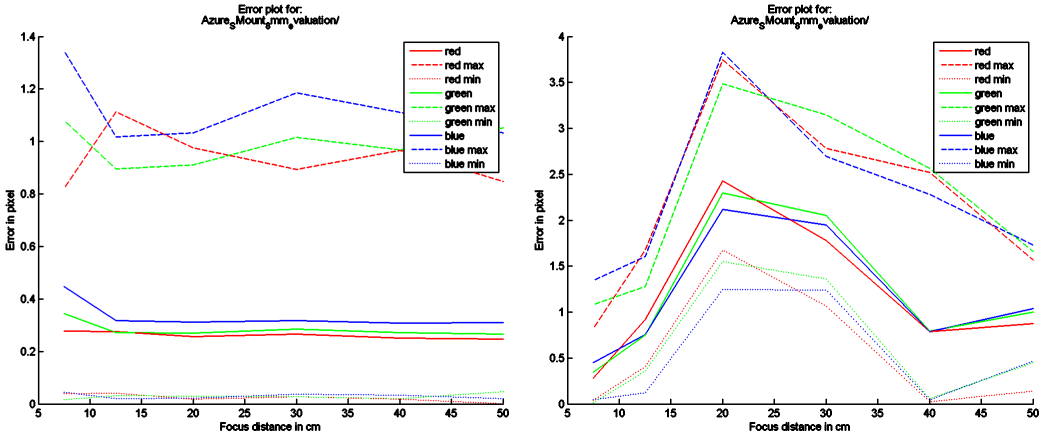

(a) CMM Measurement (b) Interpolation

Figure 5.12.: Mean error in pixel using the data of the CMM measurements for the Azure 8 mm S-Mount and the interpolation for the data.

peaks of the reprojection errors are arranged differently but the accuracies fit very well.

While the obtainable accuracy using interpolation data is not as good as for data from measurements at the specified lens setting, I urge to

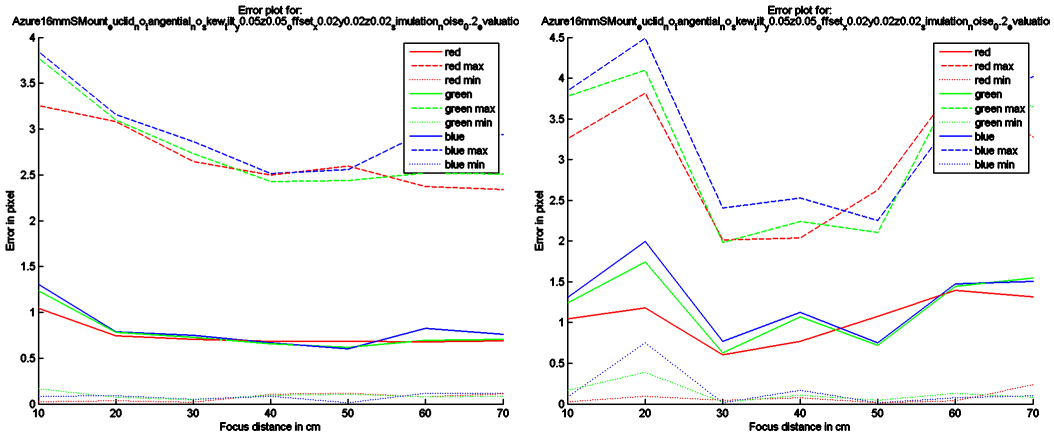

(a) Simulation (b) Interpolation

Figure 5.13.: Mean error in pixel using the data of the simulation for the Azure 16 mm S-Mount and the interpolation of the simulation data.

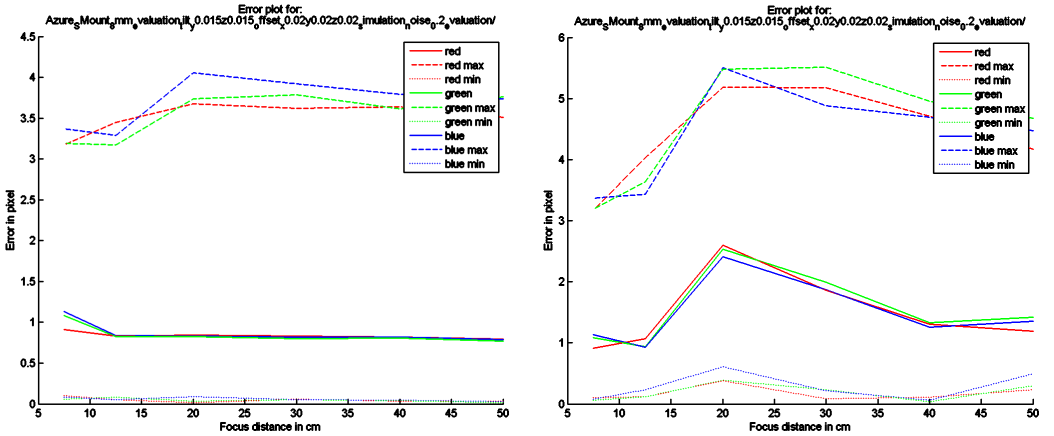

(a) Simulation (b) Interpolation

Figure 5.14.: Mean error in pixel using the data of the simulation for the Azure 8 mm S-Mount and the interpolation of the simulation data.

remember that already a small target deviation causes a similar effect or even greater loss of accuracy. One might also compare the result with respect to the alternative of using only data from one lens setting. If only a single parameter set in the middle of the inspected range is used, like

using the single parameter set of the focus 30 cm for all focus distances, the error is shown to be up to 35-45 pixels. Therefore, I consider these results very promising and the procedure a big step forward towards a more flexible camera calibration and general correction. If the processing power is available or the the time constraints chosen are different, the use of a more sophisticated interpolation method may even further increase the accuracy, which is obtainable with interpolated parameters.

5.7. Chromatic Aberration

Dealing with the chromatic aberration becomes relevant if the images of the different illumination colors are combined. To evaluate this effect reference images of two rotated squares are taken at different positions. This is done especially for the corners of an image, where the lateral chromatic aberration is expected to be most significant. The layout of the target is chosen to make the progression of the chromatic aberration more distinct. Naturally the scene needs to stay exactly the same, therefore, after a chosen position is reached, the images are taken in succession using red, green and blue illumination.

The chosen implicit correction method needs data from point correspondences, which is obtained by monochromatic illuminations experiments for red, green and blue, at a fixed camera position. All these requirements are met by the data, which is acquired for the camera calibration and lens distortion correction. Therefore, this point correspondence data can be used and no new data acquisition is necessary.

The difference in the approach, to calculate the correction for a reference channel at first, is done for green, whose wavelength is in the middle between red and blue. As explained in section 4.3, the exterior parameters of green are accordingly used to calculate the result for red and blue. Figure 5.15 shows how this leads to a more stable result for the radial parameters

The obtained parameters are used to correct the images separately, like for the monochromatic approach.

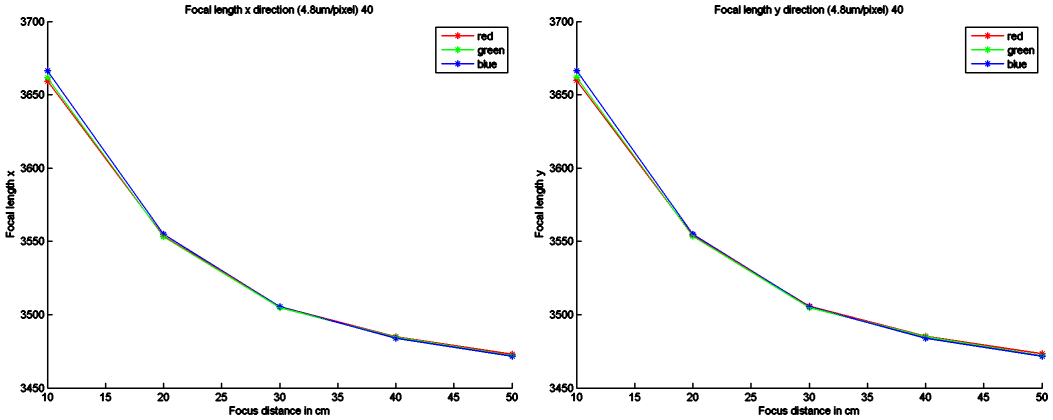

(a) f_x (b) f_y

Figure 5.15.: Fixed camera Azure 16 mm C-Mount: Horizontal and vertical focal length.

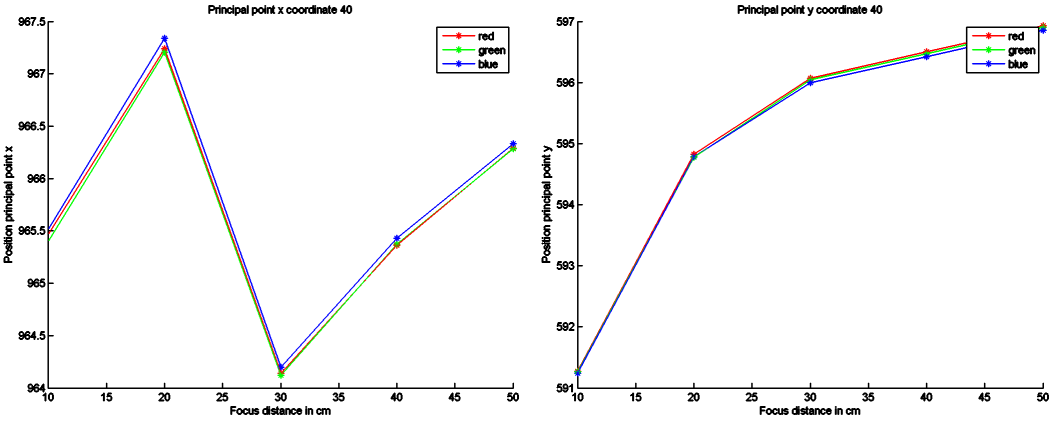

(c) c_x (d) c_y

Figure 5.15.: Fixed camera Azure 16 mm C-Mount: Principal point coordinates.

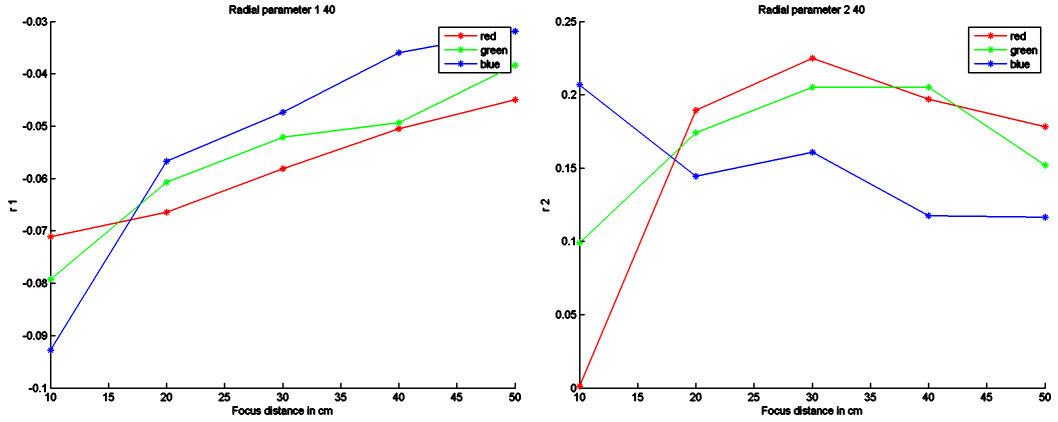

(e) r_1 (f) r_2

Figure 5.15.: Fixed camera Azure 16 mm C-Mount: Radial parameters.

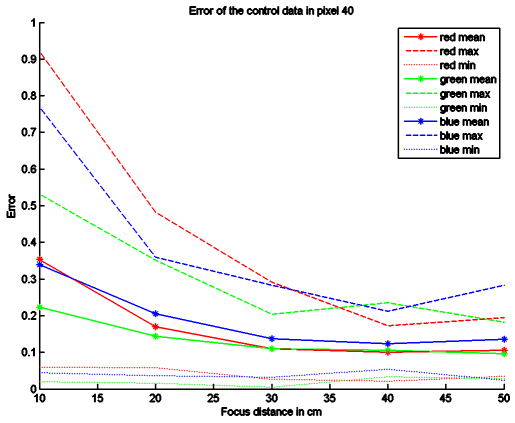

(g) Reprojection error

Figure 5.15.: Fixed camera Azure 16 mm C-Mount: Reprojection error.

Figure 5.15.: Results for the Azure C-Mount 16 mm lens evaluating the influence of a fixed camera position, using four linear and two nonlinear parameters. The camera is fixed at the position found for the green color channel. The horizontal axis of the plots show the focus distance in cm, the vertical axis the value of the parameter.

Figure 5.16 shows the the result for the correction of an image taken with the Azure 16 mm S-Mount lens. The result shows a notable improvement but figure 5.17 shows that the method does not always achieve the desired result. While the red and green channel fit pretty well, the blue channel even gets worse. The severity is exaggerated because the intensities have been manipulated to show the effect clearer but the method does not correct the image properly. The reason is presumed to be found in the iterative optimization process, which can get caught in different local minima. Sharper constraints or using the same principal point can diminish this problem but it has turned out that this also leads to a decrease in accuracy for the correction process.

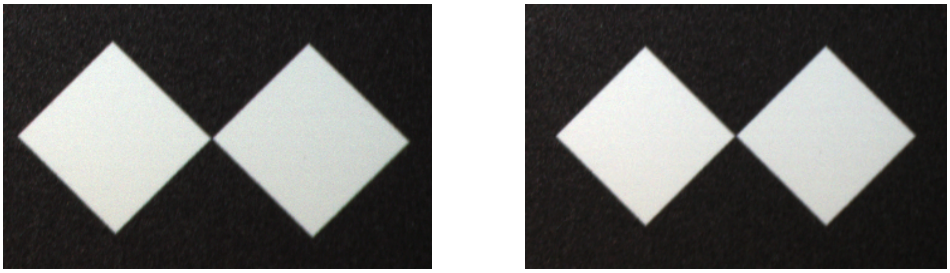

Figure 5.16.: Images using red, green and blue illumination combined to an RGB image. The target is at a distance of 50 cm and the squares on the target have a size of 15 mm. The images are taken using the Azure 16 mm Azure S-Mount lens. In the left image, the combined original image is shown. On the right side, the combined corrected image. The improvement of the corrected image can be seen at the edges of the squares.

While the whole process in general works and literature suggests it to be a good way to correct the chromatic correction effect, I find the reliability in this form lacking. An additional reason may be that the used lenses show very little chromatic aberration and, therefore, the very accurate evaluation shows limitations of the method. Otherwise the process fits the requirement for a fast method, which can be combined with the other correction methods perfectly. But it may be possible that there is a need to evaluate and adjust the details of the approach in the future.

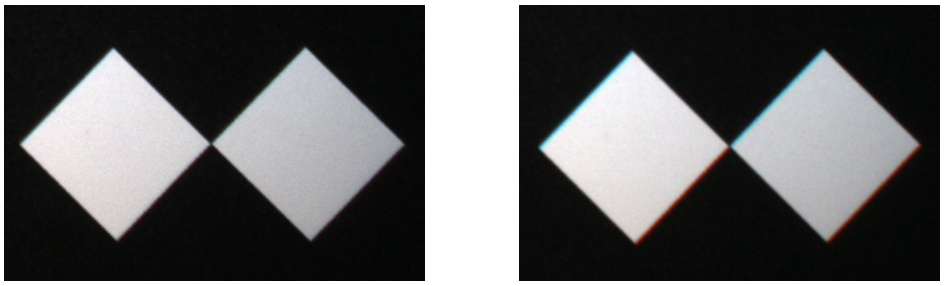

Figure 5.17.: Images using red, green and blue illumination combined to an RGB image. The target is at a distance of 50 cm and the squares on the target have a size of 15 mm. The images are taken using the Azure 8 mm Azure S-Mount lens. In the left image, the combined original image is shown. On the right side, the combined corrected image. A turquoise color fringe can be seen in the corrected image. This effect is explained in the text.

5.8. Vignetting

It it is known that the aperture has an influence on the vignetting effect but there is no information how this knowledge can be included into a flexible correction approach. Therefore, there are experiments needed to evaluate the effect more precisely. Additionally, experiments are done to evaluate the impact of the focus setting, where, to my knowledge, no information is available.

5.8.1. Vignetting setup

The setup for the acquisition of the images for the vignetting correction is simple (figure 5.18). The camera is used to take images of a homogeneous LCD display in an otherwise dark room and the results are saved on the laptop for further processing. The exposure time is adjusted to achieve maximum brightness, but to avoid overexposure. The majority of the experiments are done using an Azure 16 mm C-Mount lens, although images are taken using the Azure 8 mm and 16 mm S-Mount lenses to evaluate the general validity of the method.

Figure 5.18.: Setup for vignetting correction.

The procedure for the experiments for vignetting can be seen in figure 5.19. After the image is acquired, all processing steps are done in Matlab in the shown order. The correction is done using two and three α-terms. Experiments show that if the proposed grid contains 500 or more points, good results can be achieved.

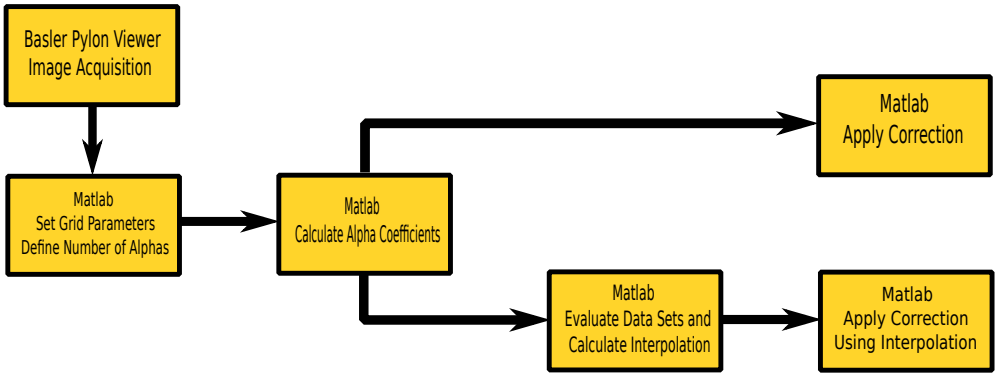

Figure 5.19.: Flowchart of the procedure for vignetting correction.

The first experiment covers the influence of the focus setting on the vignetting effect. The aperture is fixed and a new image is taken for every 10 cm. Figure 5.20 shows four example images. It is visible that the vignetting effect gets stronger with the increase of the focus distance. The necessary exposure time increases from 8250 μs for a focus distance of 70 cm to 12500 μs at 10 cm.

The second experiment addresses the aperture. Although the f-number can be adjusted continuously the usual step size is $\sqrt{2}$ which doubles the area. The minimum setting is usually an exception because of the construction limit for low f-numbers. The example images in figure 5.21 are taken at a focus setting of 30 cm using the Azure 16 mm C-Mount lens which has an aperture range from 1.8 to 16. The images show that the vignetting effect is very significant on low f-numbers and nearly disappears for high f-numbers.

During the experiments dust got caught on the filter in front of the image sensor. While this is a nuisance in general it offers a good example that the aperture has not only an impact on the depth of field on object side but on image side as well. On low f-numbers the dust is just a blurry smear, on a high f-number the structure is evident. Although interesting, the effect on the result should be minimal because of the large number of sample points.

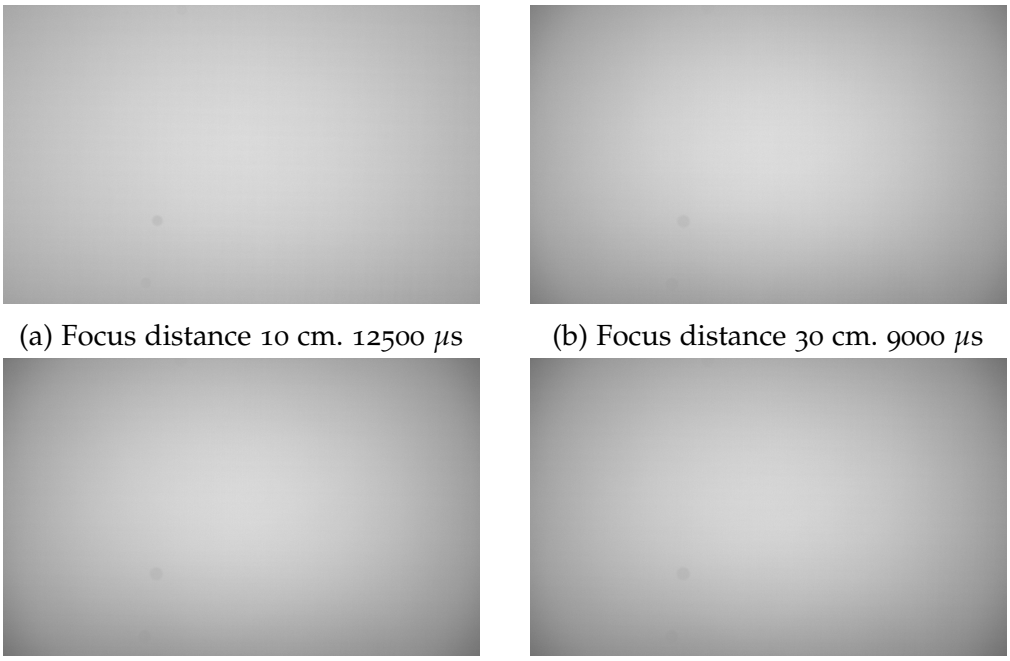

(a) Focus distance 10 cm. 12500 μs (b) Focus distance 30 cm. 9000 μs

(c) Focus distance 50 cm. 8500 μs (d) Focus distance 70 cm. 8250 μs

Figure 5.20.: The influence of different focus settings on the vignetting effect.

5.8.2. Vignetting correction

The first step in the correction process is to apply a Gauss-filter over the whole image. The low pass filter effect counteracts noise and residues from a possible Moiré effect, which may be present despite of the diffusing screen. In figure 5.22, an image before and after the filter is shown. The input image was taken before the diffusing screen was applied and shows a substantial Moiré effect. The improvement is significant and in combination with the diffusing screen the Moiré effect is virtually eliminated but this also counters possible problems with noise. An input image for an aperture setting of four and a focus distance of 30 cm is shown in figure 5.23. The result after the correction using two alpha coefficients can be seen in figure 5.24, in figure 5.25 for using three coefficients. The correction using two coefficients improves the image already significantly but the corners stay pale. This effect is a typical result for the two term correction. Using three

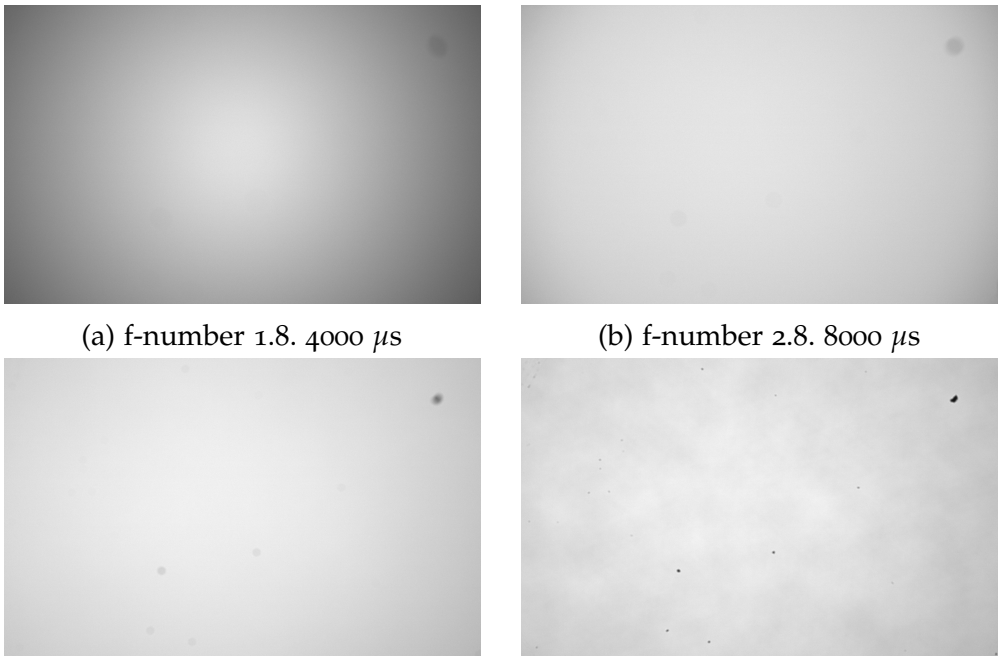

(a) f-number 1.8. 4000 μs (b) f-number 2.8. 8000 μs

(c) f-number 5.6. 32000 μs (d) f-number 16. 450000 μs

Figure 5.21.: The influence of different f-numbers on the vignetting effect.

coefficients fixes this problem and the result is considerably better, although sometimes the opposite effect occurs in which the corners are overdone. It is a general disadvantage, that the usage of three coefficients is more sensitive to produce artifacts. It is again important to note that the used correction center plays a vital role. Experiments are done using the center of the image, the centroid of pixel intensities and the principal point. The use of the principal point achieves very good and stable results. The centroid of image intensities produces reasonable results which in general are not as good as when using the principal point. The usage of the image center leads to very mixed results and can not be recommended, if another option is available.

In figure 5.26 an experiment series of eight images is analyzed using the minimum, maximum, contrast (equation 5.1) and min to max ratio of the vignetting data before and after the correction. The data supports the

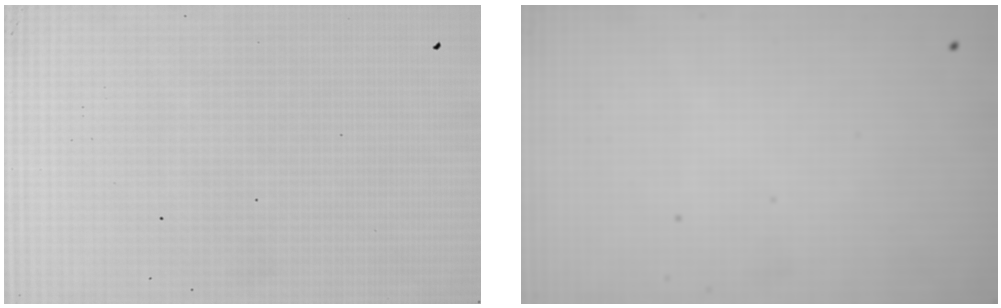

(a) Original image. (b) Image after using a Gauss filter.

Figure 5.22.: On the left side an original image showing the Moiré effect. On the right side the image after applying a Gauss filter ($size = 20$ and $\sigma = 3$). The used lens is the Azure 16 mm C-Mount.

improvement stated, although the maximum values increase more than desired.

$$contrast = \frac{I_{max} - I_{min}}{I_{max} + I_{min}} \tag{5.1}$$

Figure 5.27 shows the comparison of the corrected results using interpolated and the originally calculated alpha coefficients of an aperture experiment

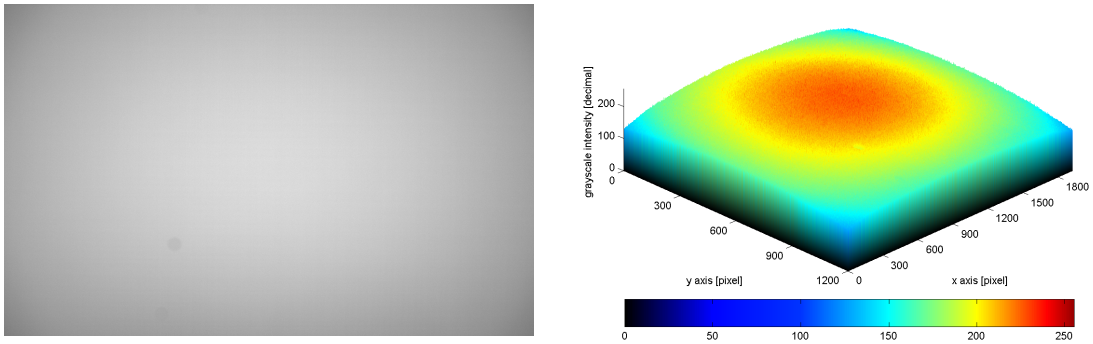

(a) Corrected image 2 terms

(b) Falsecolor 3D plot

Figure 5.23.: Original image taken for vignetting approach. The used lens is the Azure 16 mm S-Mount.

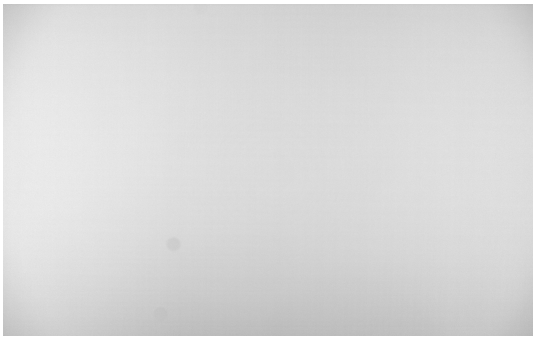

(a) Corrected image 2 terms

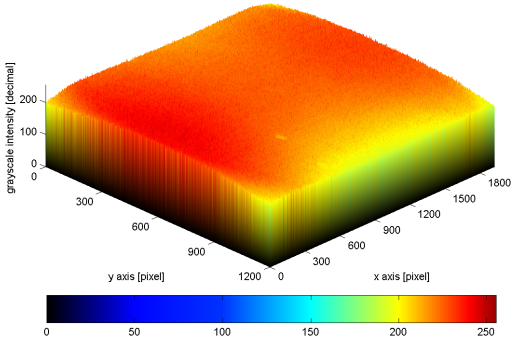

(b) Falsecolor 3D plot

Figure 5.24.: The image after a correction using two terms of equation (2.17), ($\alpha_3 = 0$). A positive effect can be seen, however, the vignetting effect is still noticeable in the corners.

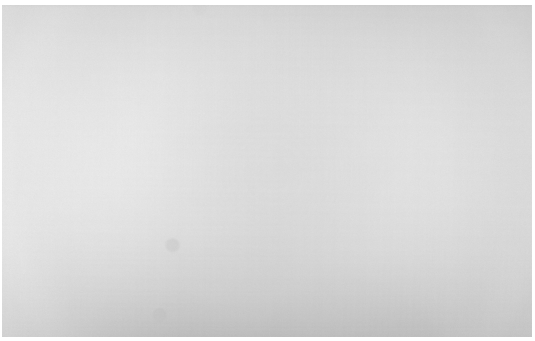

(a) Corrected image 3terms

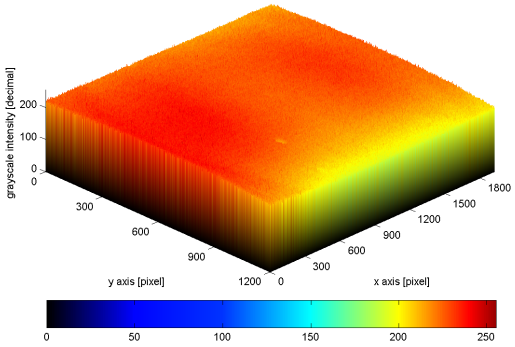

(b) Falsecolor 3D plot

Figure 5.25.: The image after a correction using all three terms of equation (2.17). The vignetting effect is no longer apparent.

series using the Azure 16 mm C-Mount lens. The interpolated parameters are calculated using linear regression. This use of interpolated coefficients leads to a correction result which usually yields a significant improvement over the original image but problems can occur if there is a position where the deviations of the dominant coefficient leads to overcompensation due to an unfavorable turn. An example of this problem can be seen in figure 5.27d where the correction leads to saturation of the image. Naturally,

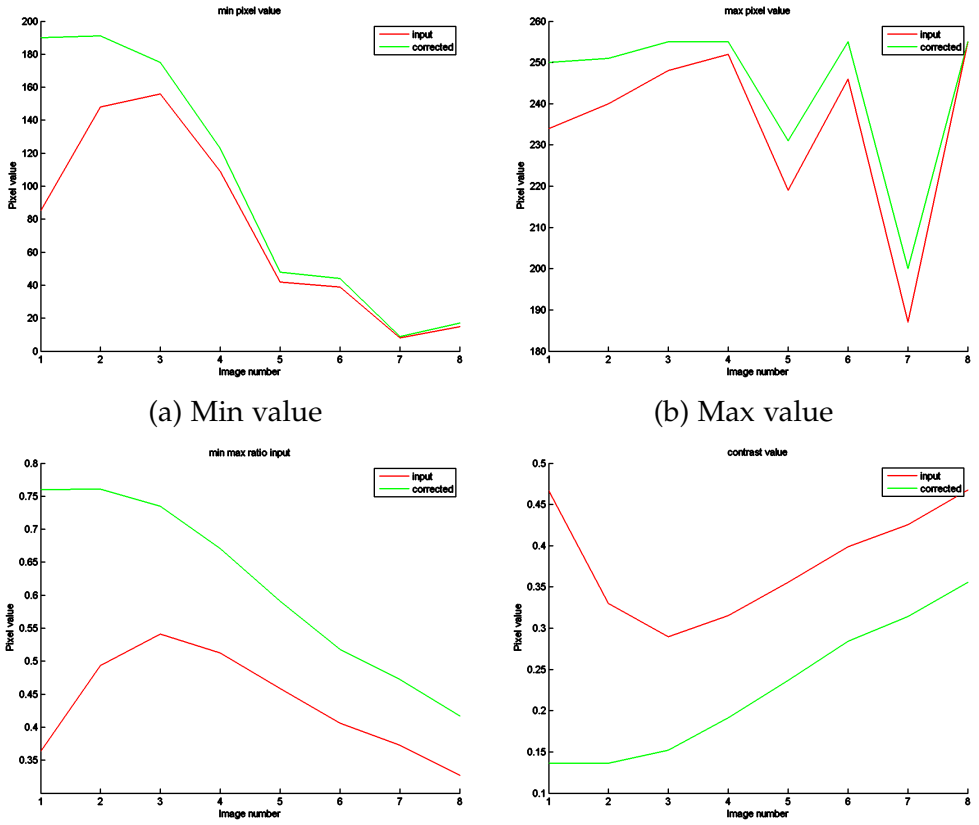

(a) Min value (b) Max value

(c) Min to max ratio (d) Contrast

Figure 5.26.: The plots of minimum and maximum pixel value, the contrast and the min to max ratio of eight images before and after vignetting correction using three terms. The plots support the increase in homogeneity after the correction.

the use of more sampling points for the interpolation can reduce this problem, especially when there are enough sample points to use a piece wise interpolation approach.

The experiments show that focus and aperture settings influence the strength of the vignetting effect significantly. At lower f-numbers the effect regarding the aperture is considerably stronger than at high f-numbers. How different focus settings influence the vignetting effect depends on the design of the lens. If the position of the internal lenses move significantly, the effect is

considerable. In the realized experiments, the increased vignetting effect for

(a) Measurement f-number 1.8.

(b) Interpolated f-number 1.8.

Figure 5.27.: Vignetting correction f-number 1.8.

(c) Measurement f-number 2.8.

(d) Interpolated f-number 2.8.

Figure 5.27.: Vignetting correction f-number 2.8.

(e) Measurement f-number 5.6.

(f) Interpolated f-number 5.6.

Figure 5.27.: Vignetting correction f-number 5.6.

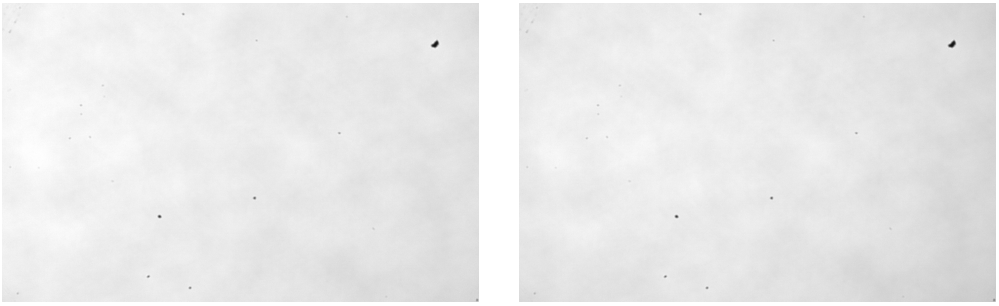

(g) Measurement f-number 16. (h) Interpolated f-number 16.

Figure 5.27.: Vignetting correction f-number 16.

Figure 5.27.: Images showing the result of a correction using the calculated parameters from the measurement data compared to parameters using linear regression as interpolation method.

a higher focus distance is already clearly visible.

The used correction methods improve the results significantly. Usually three coefficients yield the better result but depending on the used center and the used lens, the use of two coefficients can lead to a favorable result. As an example if the third coefficient tends to over correct the corners. Furthermore, the result is more stable in general if only two coefficients are used. The interpolation allows a flexible correction for each setting and leads to good results if the changes are not too sudden.

6. Conclusion

The aim of this thesis was to evaluate how many aberrations can be corrected using a fast and flexible online approach and what such an approach might look like. The results show that there are methods that can be used to correct lens distortion, chromatic aberration and vignetting in regard to that problem description very well.

Furthermore, significant parts of the solution can be built into elements of the camera calibration that is required anyway. Even the vignetting correction, where camera calibration is not mandatory, can benefit in accuracy and can use calculation synergies. While none of the methods I used is new on its own, to my knowledge, there is no research available, how lens settings like focus and aperture influence the results of camera calibration and aberration correction. There is no work describing a method that takes these settings into account, nor how all these different correction methods can be combined into a unified approach.

I have evaluated the effectiveness of the developed methods when applied to different setups, including the use of different target point clouds as well as either active or passive markers for the acquisition of point correspondences, and shown the advantages. The active target can easily be combined with the proposed three layer approach to implement a very effective and versatile acquisition method. For lens distortion and chromatic aberration, a radial model using four linear and two nonlinear parameters was found to be ideal. For vignetting, a radial model using three coefficients was found to produce the best results.

Extensive experiments with over ten thousand acquired images have shown that, to achieve accurate correction, it is absolutely necessary to take the focus and aperture settings into account and adjust the parameters accordingly. While the best result can only be achieved by obtaining parameters

for a specific setting, I have shown that – by dropping the tangential parameters and using linear regression and a hyperbola function – it is possible to interpolate the necessary parameters for camera calibration and lens correction.

The experiments show that this interpolated parameter set produces significantly better results than a single parameter set. Furthermore, since the coefficients for vignetting correction can be interpolated as well, this method is also suitable for a flexible approach.

The experiments show that the developed methods for correcting lens distortion and vignetting improve results significantly and reliably. The method used to correct chromatic aberration, however, lacks the reliability of the other two methods. Nevertheless, the results are promising enough to be confident that the residual problems can be solved with further tuning. Because all of the chosen correction methods utilize a radial model, it is possible to combine them after the parameters have been obtained.

In conclusion, although this thesis can not present solutions for every aberration listed in the introduction, it does show proof that a number of aberrations can be corrected for a large number of lens settings using fast and flexible methods. While other approaches may present more advanced methods to correct a single aberration, none have been found that offer the combination and generalization achieved in this thesis. This thesis does not present a method for correcting resolution aberrations. Existing methods for addressing this are not feasible at the moment and would need a massive increase in processing power if they were to work at all in this context.

There are a number of topics that would be interesting for follow-up work in the near future. First, it would be interesting to use a variable focal length (zoom) lens to determine how focal the length influences the various correction methods. Second, the interpolation approaches need to be confirmed for multidimensional validity, but this requires such a large number of sample points that it was infeasible for a single person in the scope of this thesis. Third, it would be helpful to know the extent to which the results are valid if extrapolated. Finally, it would be interesting to explore the possibility of applying constraints to the iterative optimization steps to prevent sudden parameter changes due to local minima without significantly decreasing the accuracy.

The last thing I would like to mention is that it should be possible and worthwhile to create an all-in-one correction solution. This means processing a single pixel at a time and applying all of the discussed correction steps for each aberration for this pixel. This would significantly reduce the number of resource-intensive calculation steps like normalization, radius and used exponents. Depending on how and in what order the correction steps are implemented, there may be side-effects that need to be detected and eliminated.

Appendix

Appendix A.

A.1. Photogrammetry

Schenk [35] states that there is no universally accepted definition of photogrammetry. In his paper he defines it as "Photogrammetry is the science of obtaining reliable information about the properties of surfaces and objects without physical contact with the objects, and of measuring and interpreting this information."

The Wikipedia article about photogrammetry[1] introduces it with "Photogrammetry is the science of making measurements from photographs, especially for recovering the exact positions of surface points." The article also mentions the definition of the American Society for Photogrammetry and Remote Sensing (ASPRS) as "... the art, science, and technology of obtaining reliable information about physical objects and the environment through processes of recording, measuring and interpreting photographic images and patterns of recorded radiant electromagnetic energy and other phenomena.".

In this thesis the focus is on the context of obtaining measurements from images but for more information the interested reader can find ample literature on the topic.

[1] https://en.wikipedia.org/wiki/Photogrammetry (14. July 2018)

A.2. Singular Value Decomposition

The singular value decomposition (SVD) (equation A.1) is a matrix factorization method. Its most common application is the solution of an overdetermined system of linear equations. The method factorizes a matrix into the three matrices, where $\boldsymbol{U}$ and $\boldsymbol{V}$ are orthogonal matrices and $\boldsymbol{D}$ is a diagonal matrix with non negative terms. This matrix $\boldsymbol{D}$ can be constructed to have its values arranged in descending order in the diagonal. If the equation system is of the form $\mathbf{Ax} = \mathbf{0}$ the solution $\mathbf{x}$ of the equation system corresponds to the smallest singular value, which is the last column of $\mathbf{V}$. If the equation system is of the form $\mathbf{Ax} = \mathbf{b}$ a vector $\mathbf{y}$ is needed: $y_i = \frac{b'_i}{d_i}$ with $\mathbf{b}' = \boldsymbol{U}^T\boldsymbol{b}$ and $\mathbf{d}$ the entries of the diagonal of $\boldsymbol{D}$). The solution then is calculated via $\mathbf{x} = \mathbf{Vy}$. A better, more precise summary, is shown in the appendix of [22].

Matrix $\boldsymbol{A}$ $m \times n$:

$$\mathbf{A} = \mathbf{UDV^T} \tag{A.1}$$

Where $\boldsymbol{U}$ is an $m \times m$ orthogonal matrix, $\boldsymbol{D}$ an $m \times n$ diagonal matrix with singular values, and $\boldsymbol{V}$ an $n \times n$ orthogonal matrix.

A.3. RQ Decomposition

The RQ-decomposition (equation A.2) decomposes a matrix $\boldsymbol{A}$ into an upper triangle matrix $\boldsymbol{R}$ and an orthonormal matrix $\boldsymbol{Q}$ (equation A.2). This calculation can be done using standard algebraic methods. For more detailed information, there is plenty of scholarly literature. As for the SVD, a good summary is provided in the appendix of [22].

The use of the standard letters $\boldsymbol{R}$ and $\boldsymbol{Q}$ is a bit confusing, because the upper triangle matrix $\boldsymbol{R}$ in camera calibration relates to the camera matrix $\boldsymbol{K}$. In contrast the second matrix $\boldsymbol{Q}$ in computer vision is named $\boldsymbol{R}$, because it describes the rotation matrix. To remove the ambiguity from the RQ-decomposition, positives entries should be enforced in the diagonal of the matrix $\boldsymbol{K}$.

RQ decomposition: $\boldsymbol{A} = \boldsymbol{RQ}$, where $\boldsymbol{R}$ denotes an upper triangle matrix and $\boldsymbol{Q}$ is an orthogonal matrix representing the three Givens rotations.

In contrast, the standard computer vision terminology for camera calibration is: $\boldsymbol{M} = \boldsymbol{KR}$, where $\boldsymbol{K}$ (interior parameters) is the upper triangle matrix, and $\boldsymbol{R}$ denotes three degree of freedom (DoF) of rotations (exterior parameters).

$$\mathbf{A} = \mathbf{RQ} \tag{A.2}$$

A.4. Bilinear Interpolation

The bilinear interpolation is a method which uses the distance of a point to its neighbors to calculate a value for this specified point. Two linear equations are used to calculate the corresponding intensity value. This can be interpreted as a linear interpolation in the first direction and then in the second direction. Although it is a combination of two linear equations it is not a linear function by itself. For image processing this means the intensity for a position is calculated from the intensity values of the surrounding pixels. The equation can be seen in equation A.3. How this relates graphically is shown in figure A.1.

$$I(x,y) = I(0,0)(1-x)(1-y) + I(1,0)x(1-y) + I(0,1)(1-x)y + I(1,1)xy \tag{A.3}$$

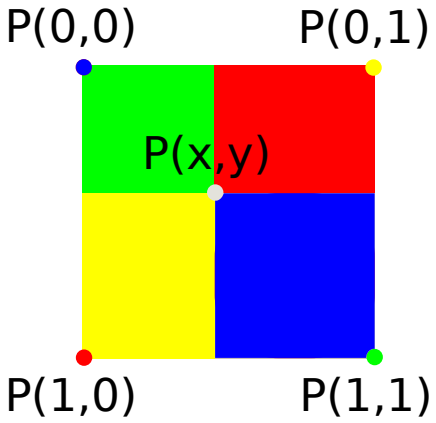

Figure A.1.: Principle of the bilinear interpolation. The value $I(x,y)$ for the point $P(x,y)$ is calculated using the value of the four adjacent neighbors P weighted by the corresponding area. In the image value and corresponding area are marked by the same color. (Equation (A.3))

Bibliography

[1] Y Abdel-Aziz and HM Karara. "Direct linear transformation into object space coordinates in close-range photogrammetry, y." In: *Proc. Symp. close-range photogrammetry, Urbana-Champaign*. 1971, pp. 1–18.

[2] Manoj Aggarwal, Hong Hua, and Narendra Ahuja. "On cosine-fourth and vignetting effects in real lenses." In: *Proc. ICCV*. Vol. 1. IEEE. 2001, pp. 472–479.

[3] Terrance E Boult and George Wolberg. "Correcting chromatic aberrations using image warping." In: *Proc. CVPR*. IEEE. 1992, pp. 684–687.

[4] Jose Henrique Brito et al. "Radial distortion self-calibration." In: *Proc. CVPR*. IEEE. 2013, pp. 1368–1375.

[5] Duane C Brown. "Close-Range Camera Calibration." In: *Photogramm. Eng* 37.8 (1971), pp. 855–866.

[6] Duane C Brown. "Decentering distortion of lenses." In: *Photometric Engineering* 32.3 (1966), pp. 444–462.

[7] Joonyoung Chang, Hee Kang, and Moon Gi Kang. "Correction of axial and lateral chromatic aberration with false color filtering." In: *IEEE Transactions on Image Processing* 22.3 (2013), pp. 1186–1198.

[8] Soon-Wook Chung, Byoung-Kwang Kim, and Woo-Jin Song. "Detecting and eliminating chromatic aberration in digital images." In: *Proc. ICIP*. IEEE. 2009, pp. 3905–3908.

[9] Timothy A Clarke and John G Fryer. "The development of camera calibration methods and models." In: *The Photogrammetric Record* 16.91 (1998), pp. 51–66.

[10] AE Conrady. "Lens-systems, Decentered." In: *Monthly notices of the royal astronomical society* 79 (1919), pp. 384–390.

[11] Frederic Devernay and Olivier Faugeras. "Straight lines have to be straight." In: *Machine vision and applications* 13.1 (2001), pp. 14–24.

[12] Colin Doutre and Panos Nasiopoulos. "Fast vignetting correction and color matching for panoramic image stitching." In: *Proc. ICIP*. IEEE. 2009, pp. 709–712.

[13] Olivier Faugeras. *Three-dimensional computer vision: a geometric viewpoint*. MIT press, 1993.

[14] Anna Fryskowska et al. "A Novel Method of Chromatic Aberration Detection and Correction Using Wavelet Analysis." In: *Proc. Baltic Geodetic Congress (BGC Geomatics)*. IEEE. 2017, pp. 18–24.

[15] Irvine C Gardner. "Validity of the cosine-fourth-power law of illumination." In: *Journal of Research of the National Bureau of Standards* 39.213-219 (1947), p. 6.

[16] Dan B Goldman and Jiun-Hung Chen. "Vignette and exposure calibration and compensation." In: *PROC. ICCV*. Vol. 1. IEEE. 2005, pp. 899–906.

[17] Richard I Hartley. "In defense of the eight-point algorithm." In: *IEEE Transactions on Pattern Analysis and Machine Intelligence* 19.6 (1997), pp. 580–593.

[18] Richard I Hartley. "Self-calibration from multiple views with a rotating camera." In: *Proc. ECCV*. Springer. 1994, pp. 471–478.

[19] Richard I Hartley. "Self-calibration of stationary cameras." In: *International journal of computer vision* 22.1 (1997), pp. 5–23.

[20] Richard Hartley and Sing Bing Kang. "Parameter-free radial distortion correction with center of distortion estimation." In: *IEEE Transactions on Pattern Analysis and Machine Intelligence* 29.8 (2007), pp. 1309–1321.

[21] Richard Hartley and Robert Kaucic. "Sensitivity of calibration to principal point position." In: *Proc. ECCV* (2002), pp. 455–456.

[22] Richard Hartley and Andrew Zisserman. *Multiple view geometry in computer vision*. 2^{nd} edition. Cambridge university press, 2003.

[23] Eugene Hecht. *Optics*. 5^{th} Global Edition. Pearson, 2016.

[24] Janne Heikkila. "Geometric camera calibration using circular control points." In: *IEEE Transactions on Pattern Analysis and Machine Intelligence* 22.10 (2000), pp. 1066–1077.

[25] Janne Heikkila and Olli Silven. "A four-step camera calibration procedure with implicit image correction." In: *Proc. CVPR*. IEEE. 1997, pp. 1106–1112.

[26] Lei Huang, Qican Zhang, and Anand Asundi. "Camera calibration with active phase target: improvement on feature detection and optimization." In: *Optics letters* 38.9 (2013), pp. 1446–1448.

[27] Neel Joshi, Richard Szeliski, and David J Kriegman. "PSF estimation using sharp edge prediction." In: *Proc. CVPR*. IEEE. 2008, pp. 1–8.

[28] Sing Bing Kang. "Automatic removal of chromatic aberration from a single image." In: *Proc. CVPR*. IEEE. 2007, pp. 1–8.

[29] Viktor Kaufmann and Richard Ladstädter. "Elimination of color fringes in digital photographs caused by lateral chromatic aberration." In: *CIPA XX International Symposium*. 2005, p. 25.

[30] John Mallon and Paul F Whelan. "Calibration and removal of lateral chromatic aberration in images." In: *Pattern Recognition Letters* 28.1 (2007), pp. 125–135.

[31] Ryuji Matsuoka et al. "Evaluation of correction methods of chromatic aberration in digital camera images." In: *ISPRS Photogrammetric image analysis* 3 (2012), p. 25.

[32] Marc Pollefeys, Reinhard Koch, and Luc Van Gool. "Self-calibration and metric reconstruction inspite of varying and unknown intrinsic camera parameters." In: *International Journal of Computer Vision* 32.1 (1999), pp. 7–25.

[33] Fabio Remondino and Clive Fraser. "Digital camera calibration methods: considerations and comparisons." In: *International Archives of Photogrammetry, Remote Sensing and Spatial Information Sciences* 36.5 (2006), pp. 266–272.

[34] Carlos Ricolfe-Viala and Antonio-Jose Sanchez-Salmeron. "Lens distortion models evaluation." In: *Applied Optics* 49.30 (2010), pp. 5914–5928.

[35] Toni Schenk. *Introduction to photogrammetry*. Course notes, The Ohio State University, Columbus, http://www.mat.uc.pt/~gil/downloads/IntroPhoto.pdf. 2005.

[36] Christoph Schmalz, Frank Forster, and Elli Angelopoulou. "Camera calibration: active versus passive targets." In: *Optical Engineering* 50.11 (2011), p. 113601.

[37] Christian J Schuler et al. "Non-stationary correction of optical aberrations." In: *Proc. ICCV*. IEEE. 2011, pp. 659–666.

[38] Ludwig Seidel. "Zur Dioptrik. Ueber die Entwicklung der Glieder 3ter Ordnung, welche den Weg eines ausserhalb der Ebene der Axe gelegenen Lichtstrahles durch ein System brechender Medien bestimmen, von Herrn Dr. L. Seidel." In: *Astronomische Nachrichten* 43.19 (1856), pp. 289–304.

[39] Warren J Smith. *Modern optical engineering*. Tata McGraw-Hill Education, 1966.

[40] Irwin Sobel. "On calibrating computer controlled cameras for perceiving 3-D scenes." In: *Artificial Intelligence* 5.2 (1974), pp. 185–198.

[41] Tiancheng Sun, Yifan Peng, and Wolfgang Heidrich. "Revisiting Cross-channel Information Transfer for Chromatic Aberration Correction." In: *Proc. CVPR*. 2017, pp. 3248–3256.

[42] Ivan E Sutherland. "Sketchpad a man-machine graphical communication system." In: *Transactions of the Society for Computer Simulation* 2.5 (1964), R–3.

[43] Roger Tsai. "A versatile camera calibration technique for high-accuracy 3D machine vision metrology using off-the-shelf TV cameras and lenses." In: *IEEE Journal on Robotics and Automation* 3.4 (1987), pp. 323–344.

[44] Robert J Vanderbei. *The Amateur Astrophotographer*. Princeton University, http://ultra.sdk.free.fr/docs/Astrophotography/references/The Amateur Astrophotographer.pdf. 2003.

[45] Guo-Qing Wei and Song De Ma. "Implicit and explicit camera calibration: Theory and experiments." In: *IEEE Transactions on Pattern Analysis and Machine Intelligence* 16.5 (1994), pp. 469–480.

[46] Reg G Willson and Steven A Shafer. "Active lens control for high precision computer imaging." In: *Proc. ICRA*. IEEE. 1991, pp. 2063–2070.

[47] Wonpil Yu, Yunkoo Chung, and Jung Soh. "Vignetting distortion correction method for high quality digital imaging." In: *Pattern Recognition, 2004. ICPR 2004. Proceedings of the 17th International Conference on*. Vol. 3. IEEE. 2004, pp. 666–669.

[48] Zhengyou Zhang. "A flexible new technique for camera calibration." In: *IEEE Transactions on Pattern Analysis and Machine Intelligence* 22.11 (2000), pp. 1330–1334.

[49] Yuanjie Zheng, S Lin, and Sing Bing Kang. "Single-Image Vignetting Correction." In: *Proc. CVPR*. Vol. 1. IEEE. 2006, pp. 461–468.

[50] Yuanjie Zheng et al. "Single-image vignetting correction from gradient distribution symmetries." In: *IEEE transactions on pattern analysis and machine intelligence* 35.6 (2013), pp. 1480–1494.

[51] Yuanjie Zheng et al. "Single-image vignetting correction using radial gradient symmetry." In: *Proc. CVPR*. IEEE. 2008, pp. 1–8.